Cell Reports

Article

Hepatocyte-macrophage crosstalk via the PGRN-EGFR axis modulates ADAR1-mediated immunity in the liver

Graphical abstract

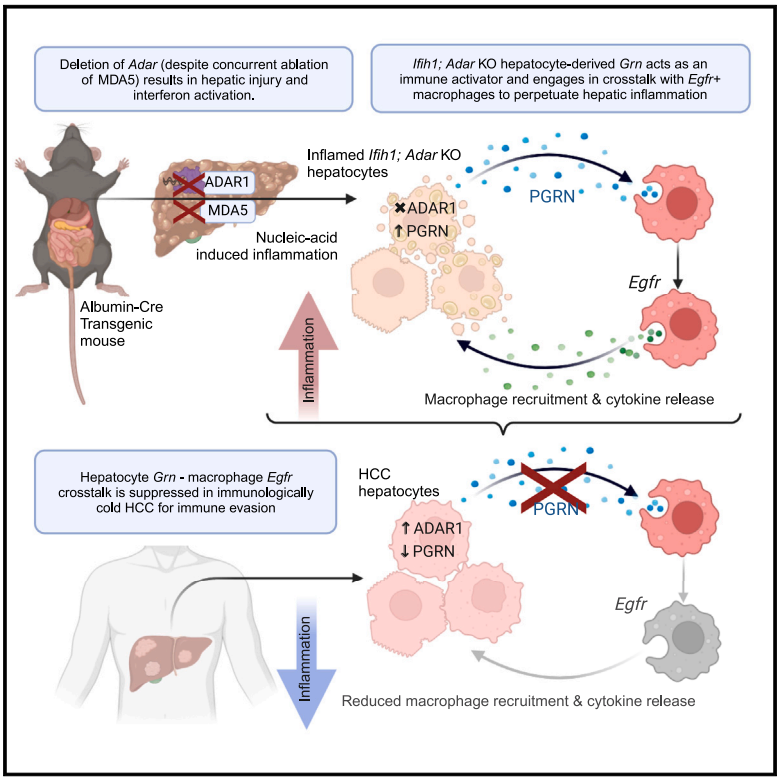

Highlights

- MDA5 loss does not rescue inflammation and dysfunction in ADAR1-deficient liver
- Tissue-specific pathways for self-dsRNA response in ADAR1-deficient liver
- PGRN mediates IFN responses and macrophage recruitment in ADAR1-deficient liver
- ADAR1 represses PGRN-EGFR signaling, promoting tumor immune evasion

Authors

Wei Liang Gan, Xi Ren, Vanessa Hui En Ng, ..., Bin Wu, Ramanuj DasGupta, Leilei Chen

Correspondence

polly_chen@nus.edu.sg

In brief

In this study, Gan et al. use multi-omics approaches to reveal that MDA5 loss in ADAR1-deficient livers does not alleviate inflammation and dysfunction. Hepatocyte-macrophage crosstalk via the PGRN-EGFR axis manages self-dsRNA responses, with PGRN mediating interferon responses and macrophage recruitment. ADAR1 suppression of PGRN-EGFR signaling aids tumor immune evasion.

Gan et al., 2024, Cell Reports *43*, 114400
July 23, 2024
https://doi.org/10.1016/j.celrep.2024.114400

CellPress

Cell Reports

CellPress
OPEN ACCESS

Article

Hepatocyte-macrophage crosstalk via the PGRN-EGFR axis modulates ADAR1-mediated immunity in the liver

Wei Liang Gan,[1,9] Xi Ren,[1,9] Vanessa Hui En Ng,[1] Larry Ng,[1] Yangyang Song,[1] Vincent Tano,[1] Jian Han,[1] Omer An,[1] Jinghe Xie,[1,2] Bryan Y.L. Ng,[1] Daryl Jin Tai Tay,[1] Sze Jing Tang,[1] Haoqing Shen,[1] Shruti Khare,[3] Kelvin Han Chung Chong,[4,5] Dan Yock Young,[1,6] Bin Wu,[4,5] Ramanuj DasGupta,[3] and Leilei Chen[1,7,8,10,*]

[1]Cancer Science Institute of Singapore, National University of Singapore, Singapore, Singapore
[2]School of Biomedical Sciences and Engineering, Guangzhou International Campus, South China University of Technology, Guangzhou, P.R. China
[3]Genome Institute of Singapore, Agency for Science Technology and Research, 60 Biopolis Street, Genome, #02-01, Singapore, Singapore
[4]School of Biological Sciences, Nanyang Technological University, Singapore, Singapore
[5]NTU Institute of Structural Biology, Nanyang Technological University, Singapore, Singapore
[6]Division of Gastroenterology and Hepatology, National University Health System, Singapore, Singapore
[7]NUS Center for Cancer Research, Yong Loo Lin School of Medicine, National University Singapore, Singapore, Singapore
[8]Department of Anatomy, Yong Loo Lin School of Medicine, National University of Singapore, Singapore, Singapore
[9]These authors contributed equally
[10]Lead contact
*Correspondence: polly_chen@nus.edu.sg
https://doi.org/10.1016/j.celrep.2024.114400

SUMMARY

ADAR1-mediated RNA editing establishes immune tolerance to endogenous double-stranded RNA (dsRNA) by preventing its sensing, primarily by MDA5. Although deleting *Ifih1* (encoding MDA5) rescues embryonic lethality in ADAR1-deficient mice, they still experience early postnatal death, and removing other MDA5 signaling proteins does not yield the same rescue. Here, we show that ablation of MDA5 in a liver-specific *Adar* knockout (KO) murine model fails to rescue hepatic abnormalities caused by ADAR1 loss. *Ifih1*;*Adar* double KO (dKO) hepatocytes accumulate endogenous dsRNAs, leading to aberrant transition to a highly inflammatory state and recruitment of macrophages into dKO livers. Mechanistically, progranulin (PGRN) appears to mediate ADAR1 deficiency-induced liver pathology, promoting interferon signaling and attracting epidermal growth factor receptor (EGFR)$^{+}$ macrophages into dKO liver, exacerbating hepatic inflammation. Notably, the PGRN-EGFR crosstalk communication and consequent immune responses are significantly repressed in ADAR1^{high} tumors, revealing that pre-neoplastic or neoplastic cells can exploit ADAR1-dependent immune tolerance to facilitate immune evasion.

INTRODUCTION

Organisms have developed sophisticated immune defenses to detect and respond to foreign or unwanted genetic materials.[1] Immunogenic molecules can come from viral genomes or be generated endogenously in various pathophysiological states. Double-stranded RNA (dsRNA) species, which can originate from viruses or cellular sources (e.g., self-derived retroelements, mitochondrially derived dsRNA), play a key role. In vertebrates, innate immune sensors detect dsRNA and trigger a multitude of immune responses. At the cellular level, cytoplasmic retinoic acid-inducible gene I (RIG-I)-like receptors, including melanoma differentiation-associated protein 5 (MDA5) and RIG-I, recognize dsRNA, activating the type I interferon (IFN) response and IFN-stimulated genes (ISGs). Although these responses are crucial for antiviral defenses to protect the organism, they must be transient and tightly regulated. Hence, nearly all organisms can distinguish between self and non-self dsRNA to reliably initiate antiviral responses.[1]

A-to-I RNA editing is catalyzed by a dsRNA-specific adenosine deaminase enzyme encoded by ADAR (adenosine deaminase that acts on RNAs) genes. ADAR1 and ADAR2 convert adenosines within duplex RNA structures to inosines. ADAR1-mediated editing marks endogenous dsRNA as "self" by altering Watson-Crick A-U base pairs to weaker I.U wobble pairs, destabilizing dsRNA and preventing its detection primarily by the MDA5-MAVS (mitochondrial antiviral signaling protein) pathway and subsequent IFN response.[2–5] Mice with null alleles of *Adar* (*Adar*$^{-/-}$) are embryonically lethal, showing widespread IFN signaling, liver disintegration, and severe hematopoietic defects.[6,7] Editing-deficient *Adar*$^{E861A/E861A}$ mice also exhibit embryonic lethality, but concurrent deletion of *Ifih1* rescues these mice to a normal lifespan.[2] In humans, ADAR1 mutations are linked to Aicardi-Goutières syndrome, a neurological

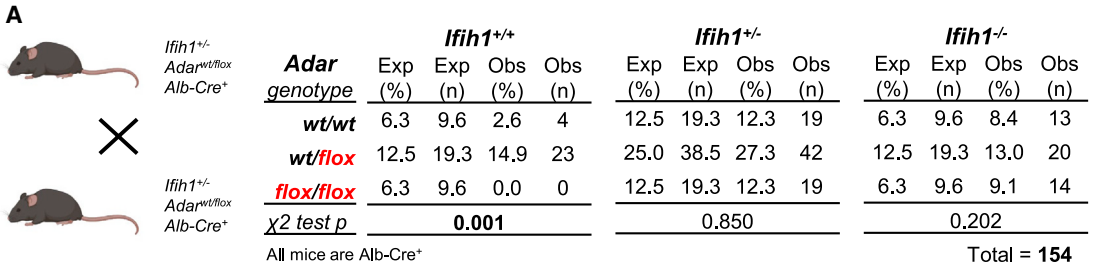

Adar genotype	Ifih1+/+ Exp (%)	Ifih1+/+ Exp (n)	Ifih1+/+ Obs (%)	Ifih1+/+ Obs (n)	Ifih1+/- Exp (%)	Ifih1+/- Exp (n)	Ifih1+/- Obs (%)	Ifih1+/- Obs (n)	Ifih1-/- Exp (%)	Ifih1-/- Exp (n)	Ifih1-/- Obs (%)	Ifih1-/- Obs (n)
wt/wt	6.3	9.6	2.6	4	12.5	19.3	12.3	19	6.3	9.6	8.4	13
wt/flox	12.5	19.3	14.9	23	25.0	38.5	27.3	42	12.5	19.3	13.0	20
flox/flox	6.3	9.6	0.0	0	12.5	19.3	12.3	19	6.3	9.6	9.1	14
χ2 test p	0.001				0.850				0.202			

Total = **154**

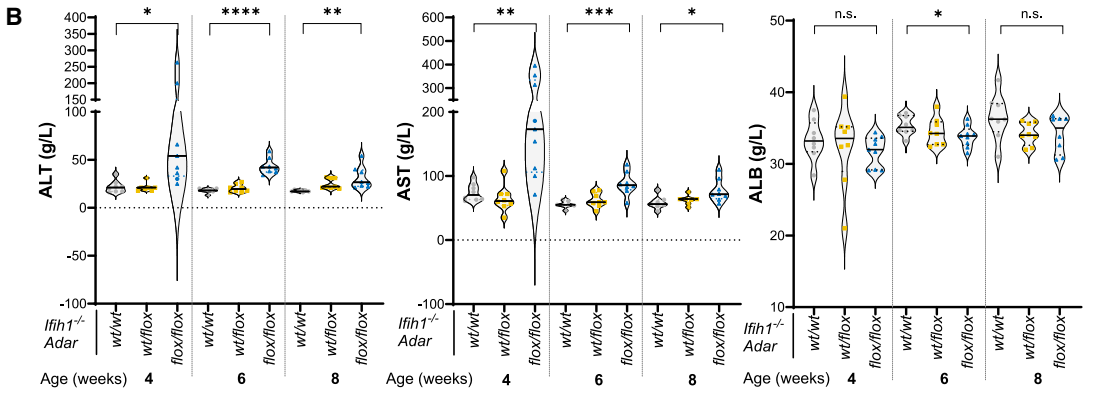

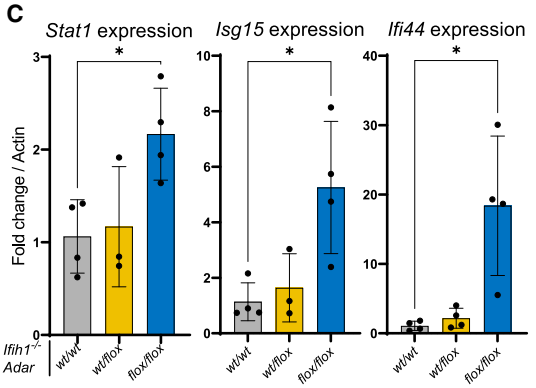

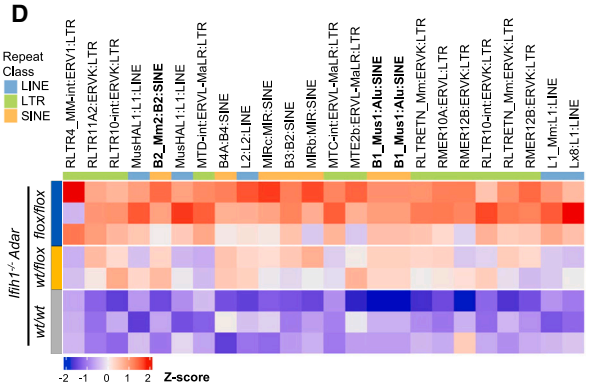

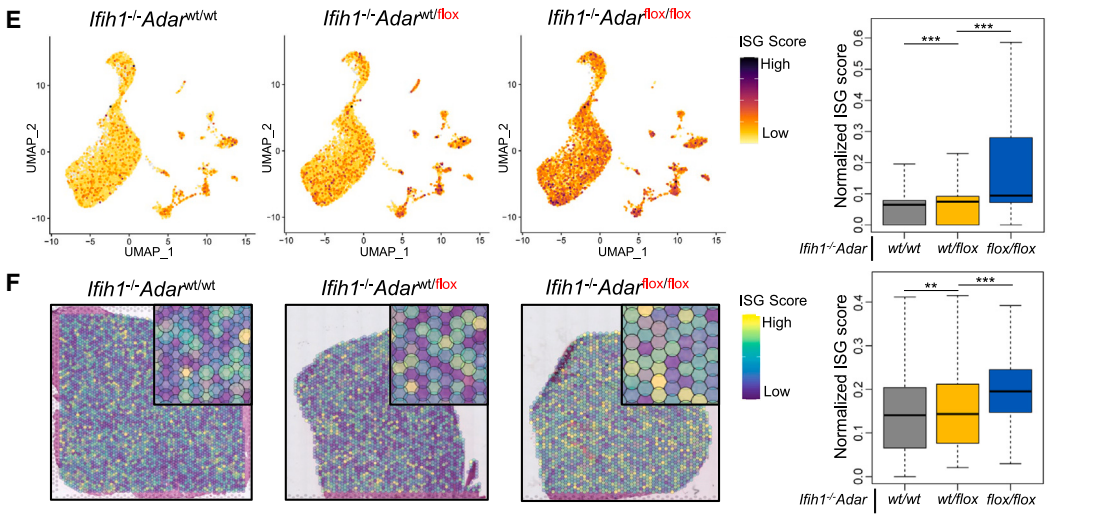

(legend on next page)

interferonopathy.[8] Collectively, ADAR1 is a major innate immune protector that suppresses the immunostimulatory activities of dsRNA and safeguards immune homeostasis. Although MDA5 is considered the primary sensor for endogenous dsRNAs following ADAR1 deficiency, concurrent deletion of MDA5 downstream signaling proteins (e.g., IRF3 or STAT1) failed to rescue, or only partially rescued (e.g., MAVS), the embryonic lethality caused by ADAR1 loss. Mice deficient in both ADAR1 and MDA5, or ADAR1 and MAVS, still underwent early postnatal death.[3,4,9] Additionally, most studies on ADAR1 and RNA editing in innate immunity have used bulk omics profiling, which lacks the single-cell resolution needed to explore intracellular and intercellular signaling changes caused by ADAR1 deficiency, hindering deeper mechanistic investigations of ADAR1-mediated immune tolerance.

ADAR1 plays a critical role in immune regulation and is functionally relevant to human diseases. Recent studies show that some cancer cells maintain subinflammatory states through immune-suppressive mechanisms like ADAR1-mediated editing.[10–12] ADAR1 is frequently upregulated in various cancer types,[13–19] likely contributing to tumor immune evasion by heavily editing endogenous dsRNA, preventing their detection and deactivating immune responses. This can lead to immunologically "cold" tumors, such as hepatocellular carcinoma (HCC).

The liver's immune system is highly tolerant to self and non-self components to maintain immune homeostasis, and loss of this tolerance can cause chronic inflammation, liver fibrosis, and cirrhosis.[20] *Adar*$^{-/-}$ embryos exhibit liver disintegration, highlighting ADAR1's essential role in liver development.[3,21] Here, we established a liver-specific *Adar* knockout (KO) mouse model and observed that homozygous deletion of *Adar* led to embryonic lethality phenocopying the full-body *Adar*$^{-/-}$ mice.[22] Although removal of *Ifih1* rescued organismal lethality, it did not rescue hepatic abnormalities induced by *Adar* loss. Leveraging bulk, single-cell, and spatial multi-omics, we show that *Ifih1*;*Adar* double KO (dKO) hepatocytes accumulated repetitive element (RE)-derived endogenous dsRNAs and aberrant transition to a highly inflammatory state, with significant changes in immunoregulatory gene expression. Progranulin (PGRN), encoded by *Grn*, was upregulated in dKO hepatocytes and was identified as not only an ISG and immune activator, but also a hepatocyte-derived ligand that recruits EGFR (epidermal growth factor receptor)-expressing (EGFR^{+}) macrophages into the diseased liver, potentiating hepatic inflammation and dysfunction. Notably, the PGRN-EGFR pathway and IFN responses were significantly repressed in ADAR1^{high} tumors. Silencing ADAR1 in HCC cells reduced tumor growth, IFN responses, and macrophage infiltration, suggesting that pre-malignant or malignant cells may hijack ADAR1-dependent immune tolerance to evade the immune system.

RESULTS

Concurrent deletion of *Ifih1* rescues embryonic lethality in liver-specific *Adar* KO mice

To study ADAR1-mediated RNA editing in the liver, we created a liver-specific *Adar* KO mouse model by crossing *Adar*$^{wt/flox}$ mice (heterozygous for an *Adar* null allele with exons 12–15 deleted) with *Alb-Cre*$^{+}$ mice (expressing Cre recombinase under the albumin promoter).[7] We crossed the resulting *Adar*$^{wt/flox}$*Alb-Cre*$^{+}$ mice with *Ifih1*$^{+/-}$ mice (carrying a heterozygous deletion of exon 1 of *Ifih1*) to observe phenotypic changes in ADAR1-deficient livers on *Ifih1*$^{+/+}$, *Ifih1*$^{+/-}$, or *Ifih1*$^{-/-}$ backgrounds (Figures S1A–S1D and S2A). *Adar* KO mice showed a significant reduction in global A-to-I editing in the livers compared to wild-type counterparts (Figure S1C). We observed that deleting *Adar* in the liver of *Ifih1*$^{+/+}$*Adar*$^{flox/flox}$*Alb-Cre*$^{+}$ mice (referred to as *Ifih1*$^{+/+}$*Adar*$^{flox/flox}$) caused embryonic lethality (Figures 1A and S2B) similar to whole-body *Adar*$^{-/-}$ mice,[22] highlighting the biological importance of ADAR1 in the liver. However, on an *Ifih1*$^{+/-}$ or *Ifih1*$^{-/-}$ background, mice were born at expected ratios (Figure 1A). *Ifih1*$^{+/-}$*Adar*$^{flox/flox}$ *Alb-Cre*$^{+}$ (referred to as *Ifih1*$^{+/-}$*Adar*$^{flox/flox}$) mice have reduced lifespans and weight compared to their *Ifih1*$^{+/-}$*Adar*$^{wt/wt}$*Alb-Cre*$^{+}$ (*Ifih1*$^{+/-}$*Adar*$^{wt/wt}$) counterparts, with 70% (28 of 40) found dead within 6 weeks (Figures S2C and S2D). *Ifih1*$^{-/-}$*Adar*$^{flox/flox}$ *Alb-Cre*$^{+}$ (*Ifih*$^{-/-}$*Adar*$^{flox/flox}$ or dKO) mice were born at the expected ratios and had normal lifespans and similar weights to *Ifih1*$^{-/-}$*Adar*$^{wt/flox}$ and *Ifih1*$^{-/-}$*Adar*$^{wt/wt}$ counterparts (Figures S2E–S2G), indicating that concurrent (heterozygous or homozygous) deletion of *Ifih1* rescues the embryonic lethality arising from liver-specific *Adar* deletion.

Ifih1;*Adar* dKO mice exhibit liver pathology

Ablation of MDA5 or MAVS resulted in limited rescue of *Adar*$^{-/-}$ mice to post-natal day 2 (P2)[3,4] or P30,[9] respectively. We

Figure 1. Phenotypic characterization of a liver-specific Adar KO murine model on the *Ifih1*$^{+/+}$, *Ifih1*$^{+/-}$, or *Ifih1*$^{-/-}$ background

(A) *Ifih1*$^{+/-}$*Adar*$^{wt/flox}$*Alb-Cre*$^{+}$ mice were bred to obtain 9 expected genotypes. Tables show the expected and observed number of live births of the indicated genotypes. Statistical analysis was performed by chi-square test within *Ifih1* groups for 154 live births. See additional information in Figure S2.

(B) Liver damage marker tracing of alanine aminotransferase (ALT) (left), aspartate aminotransferase (AST) (center), and liver functional enzyme albumin (right) in *Ifih1*$^{-/-}$*Adar*$^{wt/wt,wt/flox,\ flox/flox}$ mice. Data are represented as median, upper, and lower quartiles of 25 mice. Statistical significance is determined by unpaired, two-tailed Student's t test (*$p < 0.05$, **$p < 0.01$, ***$p < 0.001$, ****$p < 0.0001$; n.s., not significant).

(C) Bar charts showing semi-quantitative PCR of the indicated ISGs in 7-week-old mice. Data are represented as mean ± SD of ~3–4 biologically independent groups. Statistical significance is determined by unpaired, two-tailed Student's t test (*$p < 0.05$).

(D) Heatmap showing differentially expressed repetitive elements (DE-REs) in *Ifih1*$^{-/-}$*Adar*$^{flox/flox}$ livers from bulk RNA-seq. *Z* score is calculated for each of the indicated DE-REs. LINE, long interspersed nuclear element; LTR, long terminal repeat; SINE, short interspersed nuclear element.

(E) Expression of ISGs (calculated as ISG score) in uniform manifold approximation and projection (UMAP) visualization (left). Box-and-whisker plots show the ISG score in each indicated sample (right).

(F) Spatially resolved visualization of ISG score on *Ifih1*$^{-/-}$*Adar*$^{wt/wt,wt/flox,\ flox/flox}$ tissue using spatial transcriptomics. Insets show magnified views of the respective tissues (left). Box-and-whisker plots show the ISG score in each indicated sample (right).

(E and F) Data are represented as median, upper, and lower quartiles and minimum and maximum value. Statistical significance is determined by Wilcoxon rank-sum test (**$p < 0.01$, ***$p < 0.001$).

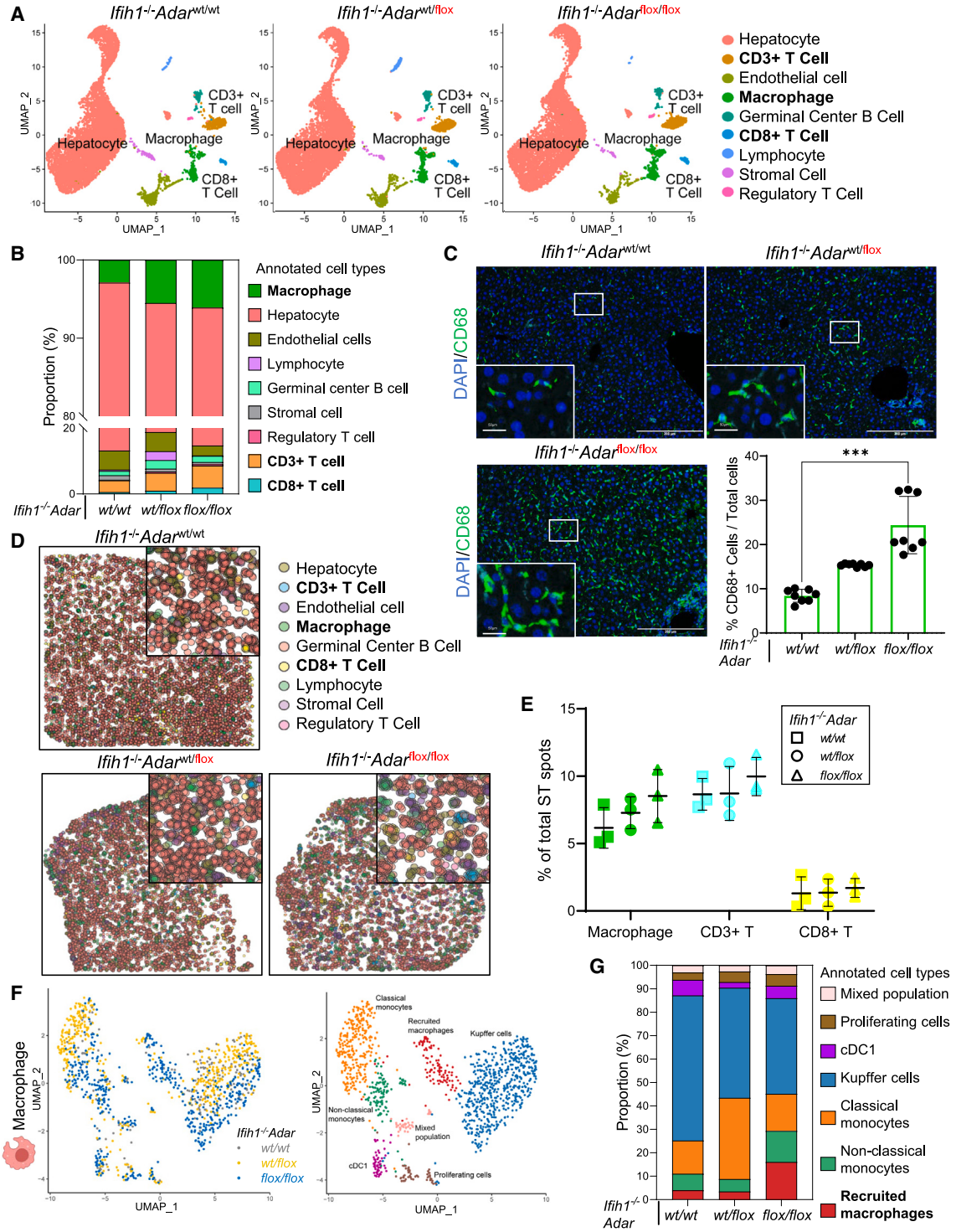

H

ID	Description	NES	FDR
GO:0002443	leukocyte mediated immunity	2.29	0.0001
GO:0043410	positive regulation of MAPK cascade	2.19	0.0005
GO:0030335	positive regulation of cell migration	2.11	0.001

(legend on next page)

wondered whether homozygous deletion of *Ifih1* could rescue hepatic abnormalities in *Ifih1*$^{-/-}$*Adar*$^{flox/flox}$ mice. Compared to *Ifih1*$^{-/-}$*Adar*$^{wt/wt}$ and *Ifih1*$^{-/-}$*Adar*$^{wt/flox}$ mice, dKO mice demonstrated disrupted liver architecture, elevated levels of liver injury markers (aspartate aminotransferase [AST] and alanine aminotransferase [ALT]), and slightly decreased total albumin levels (Figures 1B and S2H). Persistent liver pathology in *Ifih1*$^{-/-}$*Adar*$^{flox/flox}$ mice, despite MDA5 removal, suggests additional mechanisms beyond MDA5 signaling contributing to liver abnormalities in ADAR1-deficient liver.

Despite ablation of MDA5, ADAR1 loss leads to dsRNA accumulation and widespread IFN activation in hepatocytes

We conducted total (bulk) RNA sequencing (RNA-seq) analysis on liver samples from *Ifih1*$^{-/-}$*Adar*$^{flox/flox}$, *Ifih1*$^{-/-}$*Adar*$^{wt/flox}$, and *Ifih1*$^{-/-}$*Adar*$^{wt/wt}$ mice (Figure S3), which revealed distinct gene expression profiles in dKO hepatocytes, marked by activation of inflammatory type I IFN signaling (Figures S4A–S4C). This was supported by gene set enrichment analysis (GSEA) and elevated phosphorylation of STAT1, indicating Janus kinase/signal transducers and activators of transcription (JAK/STAT) signaling activation (Figures S4D and S4E). These findings demonstrate that *Ifih1*;*Adar* dKO livers underwent activation of IFN response, inflammation, and apoptosis. Persistent upregulation of ISGs (*Stat1*, *Isg15*, and *Ifi44*) was confirmed in dKO livers up to 52 weeks old (Figures 1C and S4F). However, the extent of ISG upregulation was expectedly less pronounced in dKO livers compared to *Ifih1*$^{+/-}$*Adar*$^{flox/flox}$ counterparts (Figure S4G). Despite previous studies[7,23] reporting upregulated inflammatory cytokines (e.g., interleukin-6 [IL-6], IL-8, and tumor necrosis factor alpha [TNF-α]) in liver-specific *Adar* KO mice, IL-6 and TNF-α transcripts were not significantly elevated in dKO livers (Figure S4H).

ADAR1 loss results in accumulation of unedited dsRNAs arising from REs that trigger RNA sensing and IFN response.[24] Primary *Ifih1*$^{-/-}$*Adar*$^{flox/flox}$ hepatocytes exhibited a substantial rise in cytoplasmic dsRNA compared to the other groups (Figure S5). Analysis of bulk RNA-seq data revealed significantly increased expression of consensus differentially expressed REs (DE-REs) in dKO livers (Figure 1D). Notably, *Alu*-like short interspersed nuclear elements (SINEs) elements (e.g., *B1* and *B2*), which can form long dsRNA structures and are favored by ADAR1 for RNA editing,[25] were highly upregulated in dKO livers.

To delve deeper into the alterations in dKO hepatocytes and the unique milieu and roles of hepatic immune cells, we performed droplet-based single-cell RNA-seq (scRNA-seq) on cells isolated from perfused livers and spatial transcriptomics on liver tissues (Figure S3). We analyzed 27,985 cells via scRNA-seq from *Ifih1*$^{-/-}$*Adar*$^{wt/wt}$ (9,476), *Ifih1*$^{-/-}$*Adar*$^{wt/flox}$ (9,671), and *Ifih1*$^{-/-}$*Adar*$^{flox/flox}$ (8,838) livers. These cells were classified into 14 clusters (clusters [Cl.] 0–13) and further annotated into 9 distinct cell types based on their gene expression profiles, including hepatocyte (Cl. 0, 1, 2, 3, and 9), macrophage (Cl. 6 and 8), CD3$^+$ T cell (Cl. 4), CD8$^+$ T cell (Cl. 10), regulatory T cell (Cl. 13), germinal center B cell (Cl. 7), lymphocyte (Cl. 11), endothelial cell (Cl. 5), and stromal cell (Cl. 12) (Figures S6A–S6C; Table S1). Concordant with bulk RNA-seq findings, hepatocyte clusters in *Ifih1*$^{-/-}$*Adar*$^{flox/flox}$ livers had the highest ISG expression (Figure 1E). We then analyzed the spatial localization of cell types identified from scRNA-seq using spatial transcriptomics, with each capture spot encompassing 8–15 cells (Figure S6D). Again, ISG expression was significantly higher throughout the liver tissue of *Ifih1*$^{-/-}$*Adar*$^{flox/flox}$ mice compared with the other groups, indicating widespread, non-localized hepatic inflammation in *Ifih1*;*Adar* dKO livers (Figure 1F).

ADAR1 deficiency recruits immune cells, including macrophages, into inflamed dKO liver

Various immune cells, like macrophages and T cells, are known to play important roles in liver injury, repair, and disease development.[7] From the scRNA-seq data, increased proportions of macrophages (6.1% versus 2.9%), CD3$^+$ T cells (6.7% versus 3.5%), and CD8$^+$ T cells (1.9% versus 0.6%) were observed in *Ifih1*$^{-/-}$*Adar*$^{flox/flox}$ livers compared to *Ifih1*$^{-/-}$*Adar*$^{wt/wt}$ (Figures 2A and 2B). Immunofluorescent or immunohistochemical staining confirmed these findings (Figures 2C and S7A). Using the Cell-type Identification By Estimating Relative Subsets Of RNA Transcripts (CIBERSORT) algorithm[26] to estimate cell type composition from bulk RNA-seq data (Figure S7B) and mapping cell types identified from scRNA-seq to their spatial positions on liver tissues using CellTrek deconvolution of spatial transcriptomics data[27] (Figures 2D and 2E), macrophages were consistently identified as the cell type dramatically enriched in dKO livers compared to other cell types. Macrophages in *Ifih1*$^{-/-}$*Adar*$^{flox/flox}$ livers were highly activated compared to those in *Ifih1*$^{-/-}$*Adar*$^{wt/wt}$ livers, exhibiting xenobiotic catabolic processes, ion transportation, and glutathione derivative biosynthesis (Figure S7C). Importantly, sodium uptake and glutathione production promote pro-inflammatory macrophage functions like phagocytosis and superoxide production, potentially exacerbating hepatic injury.[28–30]

Figure 2. ADAR1 loss recruits immune cells, including activated macrophages, into inflamed dKO liver

(A) UMAP visualization and cell type annotation for the indicated *Ifih1*$^{-/-}$*Adar*$^{wt/wt,wt/flox,\ flox/flox}$ livers from scRNA-seq.

(B) Parts-of-whole plot showing proportions of cell types annotated in (A) in the indicated liver samples.

(C) Representative immunofluorescent detection of CD68 (macrophage). Inset: magnified view of the boxed region. A bar plot shows the percentage of CD68$^+$ cells. Data are represented as mean ± SD of 8 fields. Statistical significance is determined by unpaired, two-tailed Student's t test (***$p < 0.001$). Scale bar, 200 μm. Inset scale bar, 50 μm.

(D) Spatial mapping of cell types in *Ifih1*$^{-/-}$*Adar*$^{wt/wt,wt/flox,\ flox/flox}$ livers using CellTrek. Inset: magnified view.

(E) Scatterplot showing proportions of each cell type present in the indicated livers described in (D). Data are represented as mean ± SD of 3 planes of tissue.

(F) UMAP visualization of sub-clustered macrophages in *Ifih1*$^{-/-}$*Adar*$^{wt/wt,wt/flox,\ flox/flox}$ livers (left) and immunophenotyping of macrophage subtypes (right).

(G) Parts-of-whole plot showing proportions of macrophage subtypes across *Ifih1*$^{-/-}$*Adar*$^{wt/wt,wt/flox,\ flox/flox}$ livers.

(H) Table showing gene set enrichment analysis (GSEA) comparing the recruited macrophage subcluster to all other macrophage subclusters. Normalized enrichment score and false discovery rate (FDR)-adjusted *p* value (FDR q value) are shown.

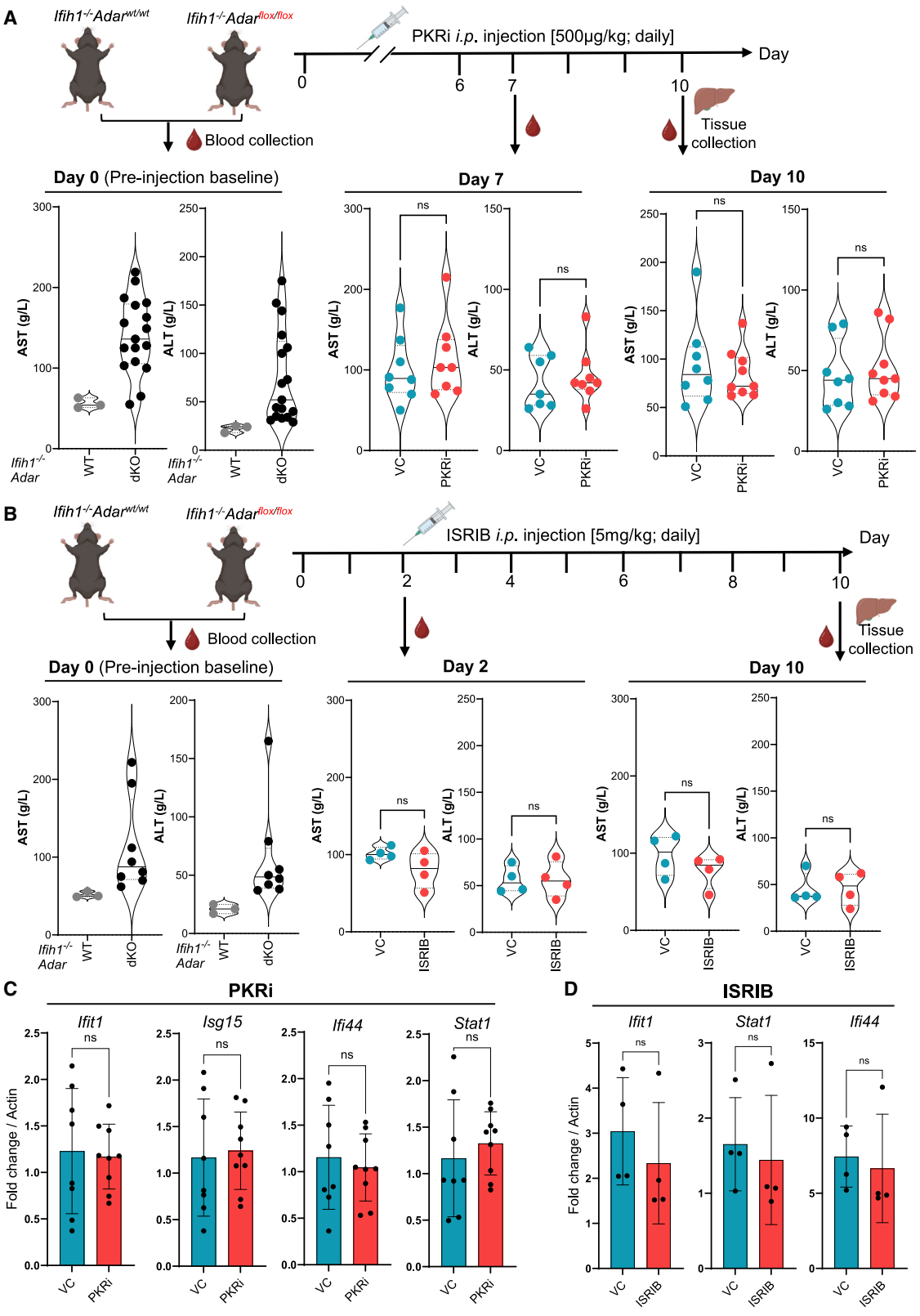

(legend on next page)

We next conducted immunophenotyping by subclustering macrophages from scRNA-seq data (Figures 2F and S7D). Strikingly, we observed an increased proportion of recruited macrophages, but not resident Kupffer cells, in dKO livers (Figures 2F and 2G). Notably, these recruited macrophages displayed pro-inflammatory transcription programs (Figure 2H). Collectively, *Ifih1*$^{-/-}$*Adar*$^{flox/flox}$ livers exhibit typical signs of innate immune activation, including ISG upregulation and the recruitment of activated macrophages.

Canonical dsRNA sensing mechanisms likely do not contribute to ADAR1-deficient liver pathology

Recent studies show that, in the absence of ADAR1, unedited dsRNAs can activate MDA5/MAVS/IRF3, protein kinase R/eukaryotic translation initiation factor 2A (PKR/EIF2α), 2′-5′-oligoadenylate synthetase/ribonuclease L (OAS/RNAse L) signaling from A-RNA (right-handed dsRNA) and Z-DNA binding protein 1/receptor-interacting protein 3/Mixed Lineage Kinase Domain-Like Pseudokinase (ZBP1/RIP3/MLKL)-driven necroptosis from Z-RNA (left-handed dsRNA).[2,10–12,31,32] However, we did not observe IRF3 phosphorylation, ZBP1/RIP3/MLKL signaling, significant increases in PKR/EIF2α phosphorylation, or OAS/RNAse L-mediated RNA cleavage in *Ifih1*$^{-/-}$*Adar*$^{flox/flox}$ livers compared to the other groups (Figures S8A–S8C). This may be attributable to low expression of *Zbp1, Ripk3*, *Eif2ak2* (PKR), *Eif2a*, *Oas1a*, and *Rnasel* in mouse livers compared to other tissues like skin and intestine[32–35] (Figure S8D). Recent studies highlight MDA5 and PKR as key immune sensors of the fatal autoinflammation following ADAR1 deficiency.[36,37] However, PKR signaling was not selectively activated in dKO livers. We did not observe consistent upregulation of integrated stress response (ISR) genes (e.g., *Asns* and *Hmox1*), which indicate EIF2α phosphorylation, by bulk RNA-seq (Figure S8E) or qPCR (Figure S8F). Furthermore, treatment of primary dKO hepatocytes with an ISR inhibitor (ISRIB) or PKR inhibitor (PKRi) did not significantly suppress ISG expression (Figures S9A and S9B). Prolonged inhibition of PKR signaling or ISR activation with high doses of PKRi or ISRIB in *Ifih1*$^{-/-}$*Adar*$^{flox/flox}$ mice also failed to significantly reduce liver damage markers or abolish ISG upregulation in dKO livers (Figures 3A–3D, S9C, and S9D). These results demonstrated that, during ADAR1 deficiency, canonical dsRNA sensing mechanisms involving IRF3, PKR/EIF2α, ZBP1, and OAS/RNAse L are unlikely to contribute to liver pathology, indicating the cell type and tissue specificity of RNA sensing pathways.

PGRN activates inflammatory response and mediates hepatocyte-macrophage interaction in dKO livers

To study dynamic changes in dKO hepatocytes and identify key immunoregulatory factors recruiting macrophages into the dKO liver, we utilized our scRNA-seq data for RNA velocity analysis of hepatocytes.[38] Among 5 hepatocyte clusters identified from scRNA-seq data (Figures 4A and S6A), Cl. 0 and Cl. 1 hepatocytes in dKO livers (the majority) demonstrated a clear transition toward Cl. 3. No evident cell state transition occurred in *Ifih1*$^{-/-}$*Adar*$^{wt/wt}$ livers, with *Ifih1*$^{-/-}$*Adar*$^{wt/flox}$ hepatocytes exhibiting an intermediate state (Figure 4A). Moreover, the Cl. 3 subpopulation was enriched in dKO livers (14.0%) compared to *Ifih1*$^{-/-}$*Adar*$^{wt/wt}$ (8.6%) and *Ifih1*$^{-/-}$*Adar*$^{wt/flox}$ (8.4%) (Figure 4A). ‘‘Immune system process’’ is the most significantly enhanced Gene Ontology (GO) term among the significantly upregulated genes in Cl.3 dKO hepatocytes (dKO-Cl.3-SUGs) (Figure S10A; Tables S2 and S3). Unlike the low expression of canonical dsRNA sensing pathway genes (e.g., *Zbp1*, *Ripk3*, *Eif2ak2*, *Eif2a*, and *Oas1a*; Figure S8D), most dKO-Cl.3-SUGs linked to immune regulation (e.g., *Ifitm3*, *C4bp*, *Cfh*, and *Grn*) showed substantial or moderate expression in mouse livers compared to other tissues (Figure S8D; Table S4), implying their likely involvement in liver immune regulation.

We next performed cell-cell interaction analysis of scRNA-seq data using NicheNet[39] to explore differentially enhanced hepatocyte-macrophage communications in dKO livers. We observed multiple outgoing signals from hepatocytes (Figure 4B, y axis), reflecting their ability to simultaneously activate macrophages in dKO livers (Figure 4B, x axis). Among the top inferred interactions (dotted-line box, Figure 4B), PGRN (encoded by *Grn*) was identified as a key hepatocyte-derived ligand forming a ligand-receptor pair with EGFR^{+} macrophages in dKO livers. PGRN expression was elevated across all dKO hepatocyte clusters, with Cl. 3 showing the most prominent increase (highlighted as one of the dKO-Cl.3-SUGs) (Figures 4C, S10B, and S10C; Table S2). Concordantly, elevated expression of *Grn* and *Egfr* was observed in hepatocytes and macrophages, respectively, in dKO livers (Figures S10D and S10E). *Grn* encodes PGRN, a stress-induced glycoprotein involved in inflammation and wound healing, and is implicated in inflammatory autoimmune diseases,

Figure 3. Prolonged inhibition of PKR signaling and ISR activation does not rescue dKO mice from hepatic inflammation and injury

(A) Schematic illustrating PKR inhibitor (PKRi) administration to dKO mice. Blood was first collected from *Ifih1*$^{-/-}$*Adar*$^{wt/wt}$ (wild type [WT]) (n = 3) and *Ifih1*$^{-/-}$*Adar*$^{flox/flox}$ (dKO) (n = 17) mice for measurement of liver damage markers prior to the first intraperitoneal (i.p.) injection of PKRi to dKO mice. dKO mice were injected daily with 500μg/kg PKRi. Blood was collected on days 7 and 10, and mice were sacrificed at day 10 for liver tissue collection (top). The liver damage markers ALT, and AST were measured in serum of dKO mice injected with either vehicle control (VC) or PKRi. Data are represented as median with upper and lower quartiles of 17 mice.

(B) Schematic illustrating ISRIB administration to dKO mice. Blood was first collected from *Ifih1*$^{-/-}$*Adar*$^{wt/wt}$ (WT) (n = 3) and *Ifih1*$^{-/-}$*Adar*$^{flox/flox}$ (dKO) (n = 8) mice for measurement of liver damage markers prior to the first i.p. injection of ISRIB to dKO mice. dKO mice were injected daily with 5 mg/kg ISRIB. Blood was collected on days 2 and 10, and mice were sacrificed at day 10 for liver tissue collection (top). ALT and AST were measured in serum of dKO mice injected with VC or ISRIB. Data are represented as median with upper and lower quartiles of 8 mice.

(C) Bar plots showing qPCR of ISG expression in dKO mice injected with either VC or PKRi. Data are represented as mean ± SD of 8–9 biological replicates per group.

(D) Bar plots showing qPCR of ISG expression in dKO mice injected with either VC or ISRIB. Data are represented as mean ± SD of 4 biological replicates per group.

Statistical significance is determined by unpaired, two-tailed Student’s t test.

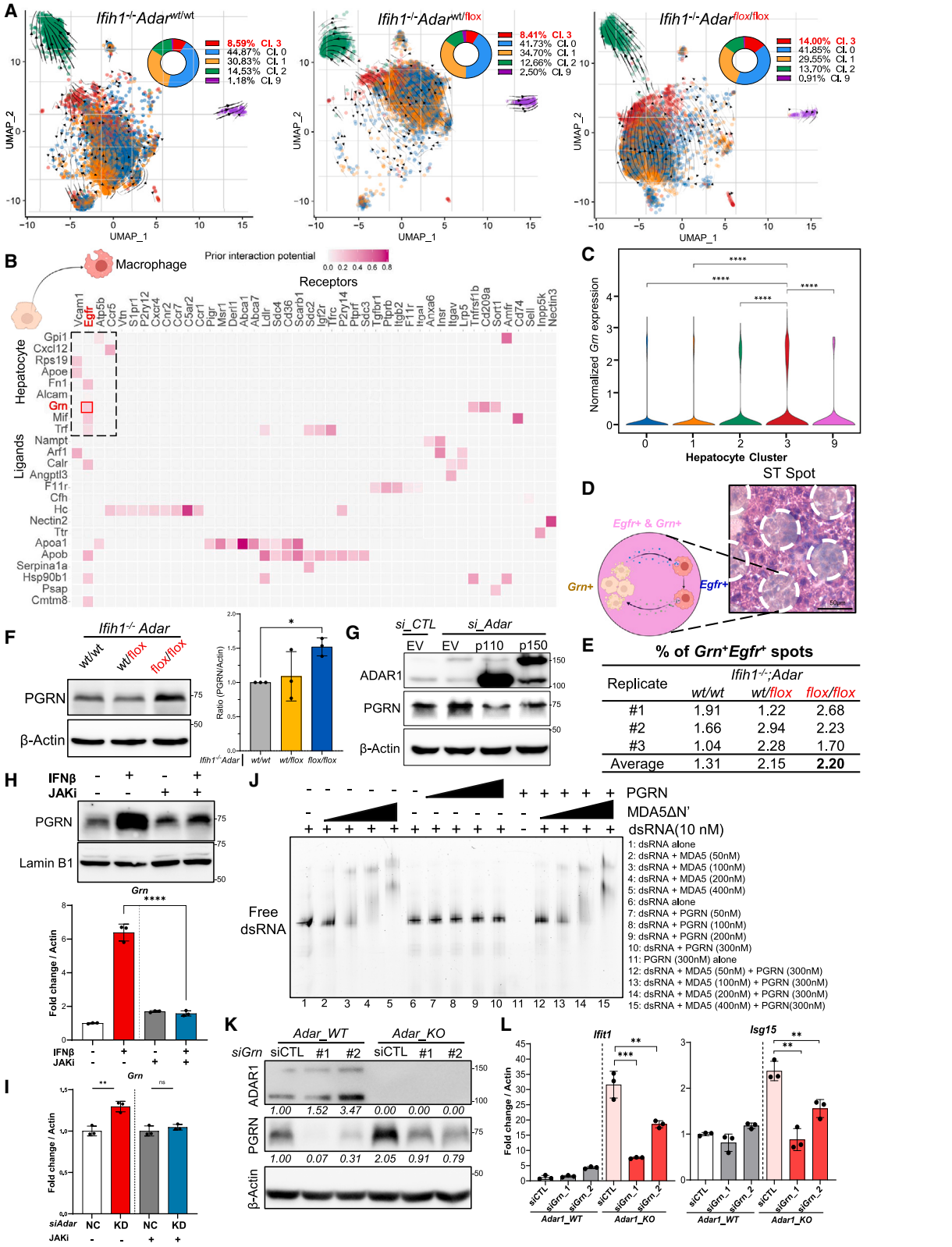

(legend on next page)

cancer, and neurological diseases.[40] PGRN can signal extracellularly, interacting with various receptors on diverse cell types, including EGFR,[41] an important regulator of macrophage activation.[42] Furthermore, the mitogen-activated protein kinase signaling cascade, a downstream pathway of EGFR, was activated in recruited macrophages in dKO livers (Figure 2H), supporting the *Grn-Egfr* communication.

We investigated whether PGRN-expressing ($PGRN^+$) hepatocytes and $EGFR^+$ macrophages were in close spatial proximity. Each spatial transcriptomics (ST) spot was defined as a microregion comprising 8–15 closely interacting cells, with only those containing macrophages included for analysis (Figures 4D and S6D). Among the macrophage-containing microregions, dKO livers had the highest number of microregions where $PGRN^+$ hepatocytes and $EGFR^+$ macrophages were closely situated (pink spots, Figures 4D, 4E, and S10F). These findings suggest that the PGRN-EGFR intercellular communication was differentially activated in dKO liver, indicating that upregulation of immunoregulatory factors like PGRN in ADAR1-deficient hepatocytes can mediate inflammatory responses and recruit $EGFR^+$ macrophages into the dKO liver.

Grn is induced by IFN signaling and subsequently intrinsically promotes IFN responses in ADAR1-deficient hepatocytes

PGRN-EGFR emerged as a prominent intercellular communication (Figures 4B–4E and S10B–S10F). It is plausible that, during breakdown of self-tolerance, *Adar*-deficient hepatocytes upregulate *Grn*, leading to PGRN production and release into the hepatic milieu, recruiting $EGFR^+$ macrophages. To test this, we validated the increased PGRN levels in primary dKO hepatocytes (Figures 4F and S11A). We found that restoring ADAR1 expression (both p110 and p150 isoform) in ADAR1 knockdown (ADAR1-KD) AML12 murine hepatocytes suppressed the upregulation of *Grn* and ISG genes (Figures 4G and S11B). Additionally, treatment of AML12 hepatocytes with either poly(I:C) (a synthetic analog of viral dsRNA) or IFNβ upregulated PGRN and *Isg15* in a dose-dependent manner (Figures S11C and S11D). The induction of *Grn* and ISG expression by IFNβ was largely abolished by a JAK inhibitor (JAKi), which inhibits type I IFN receptor signaling (Figures 4H and S11E). These findings suggested that *Grn* is an ISG responsive to type I IFN signaling activated by dsRNA or IFN receptors. Upregulation of *Grn* by ADAR1 KO was evident regardless of MDA5 presence (Figure S11F). JAKi treatment showed that ADAR1 depletion in AML12 hepatocytes could not upregulate *Grn*, indicating that ADAR1 loss upregulates *Grn* via IFN signaling (Figures 4I and S11G). Further analyses revealed that PGRN protein does not directly bind to dsRNA probes (Figure 4J, lanes 6–10). Additionally, the binding of purified MDA5ΔN' protein, which retains MDA5's intact RNA binding affinity and ATP hydrolysis activity,[43] to dsRNA probes was unaffected by PGRN (Figure 4J, lanes 1–5 vs. lanes 11–15). Altogether, ADAR1 loss reliably upregulates the ISG *Grn* in the liver through IFN signaling, irrespective of MDA5 presence.

Next, we examined the impact of PGRN in hepatocytes with ADAR1 deficiency by silencing *Grn* in ADAR1-KO or KD AML12 murine hepatocytes and primary dKO hepatocytes. In all models with ADAR1 depletion, upregulation of *Ifit1* and *Isg15* was consistently observed, which was attenuated by *Grn* depletion (Figures 4K, 4L, S11H, S11I, and 5E). These findings suggest that ADAR1 loss in the liver activates IFN signaling, leading to *Grn* upregulation, which promotes IFN responses in hepatocytes.

Figure 4. *Ifih1;Adar* dKO hepatocytes engage macrophages in crosstalk signaling via PGRN, an ISG and an immune activator that intrinsically promotes IFN responses in dKO hepatocytes

(A) RNA velocity plot UMAP showing the predicted direction of cell-state transition (indicated by arrowheads) for subclustered hepatocytes (Cl. 0, 1, 2, 3, and 9) from $Ifih1^{-/-}Adar^{wt/wt,wt/flox,\ flox/flox}$ livers. Respective proportions of hepatocyte subclusters are shown as parts-of-whole plots. Subclustered hepatocyte Cl. 0, 1, 2, 3, and 9 correspond directly to hepatocyte clusters from cell type annotation shown in Figure S6A.

(B) Heatmap showing the candidate differentially activated cell-cell in dKO livers compared to $Ifih1^{-/-}Adar^{wt/wt}$ and $Ifih1^{-/-}Adar^{wt/flox}$ livers, using NicheNet. Top intercellular communication pairs are highlighted by a dotted-line box. See further descriptions in STAR Methods.

(C) Violin plot showing normalized expression of *Grn* in hepatocyte subclusters from scRNA-seq. Statistical significance is determined by Wilcoxon rank-sum test (****$p < 0.0001$).

(D) Schematic illustrating interaction between *Grn*-expressing hepatocytes and *Egfr*-expressing macrophages in the ST microregion. See further descriptions in Figure S10F.

(E) Percentage of double-positive ST spots among all identified macrophage-containing ST spots described in (D) for the indicated tissue sections.

(F) Western blot detection of PGRN in the indicated livers (left). Bar charts showing the ratio of PGRN band intensity to actin, normalized to $Ifih1^{-/-}Adar^{wt/wt}$ (right). Data are represented as mean ± SD of 3 biological replicates.

(G) Western blot detection of the indicated proteins in AML12 cells co-transfected with control small interfering RNA (siRNA) (si_CTL) or *Adar*-targeting siRNA (si_Adar), along with empty vector or the *Adar* p110 or p150 (p110 or p150) expression construct. See supporting data in Figure S11B.

(H) Western blot detection of PGRN in AML12 cells treated with 0 (−) or 1,000 (+) units/mL of IFNβ and VC (−) or JAK inhibitor (JAKi) (+). Lamin B1 was used as a loading control (top). A bar plot shows qPCR of *Grn*. Data are represented as mean ± SD of 3 technical replicates (bottom). See supporting data in Figure S11E.

(I) Bar plot showing qPCR of *Grn* in AML12 cells transfected with *Adar*-targeting siRNA (KD) or control siRNA (NC) treated with either VC (−) or JAKi (+). Data are represented as mean ± SD of 3 technical replicates. See supporting data in Figure S11G.

(J) RNA electrophoretic mobility shift assay analysis of the binding of purified MDA5ΔN' protein to the indicated *BRI3BP* dsRNA probes in the absence or presence of PGRN protein. A representative image is shown for 3 independent experiments employing *in vitro* synthesized BRI3BP probes and 3 separate batches of freshly purified MDA5ΔN' protein.

(K) Western blot analysis of the indicated proteins in ADAR1 knockout (*Adar*_KO) or control (*Adar*_WT) AML12 hepatocytes co-transfected with siGrn_1, siGrn_2, or siCTL. The signal intensity (ratio to actin) of the respective proteins is shown, normalized to siCTL-treated AML12 *Adar*_WT cells.

(L) Bar charts showing qPCR of *Ifit1* or *Isg15* in samples described in (K). Data are represented as mean ± SD of 3 technical replicates.

(F–L) Statistical significance is determined by unpaired, two-tailed Student's t test (*$p < 0.05$, **$p < 0.01$, ***$p < 0.001$, ****$p < 0.0001$).

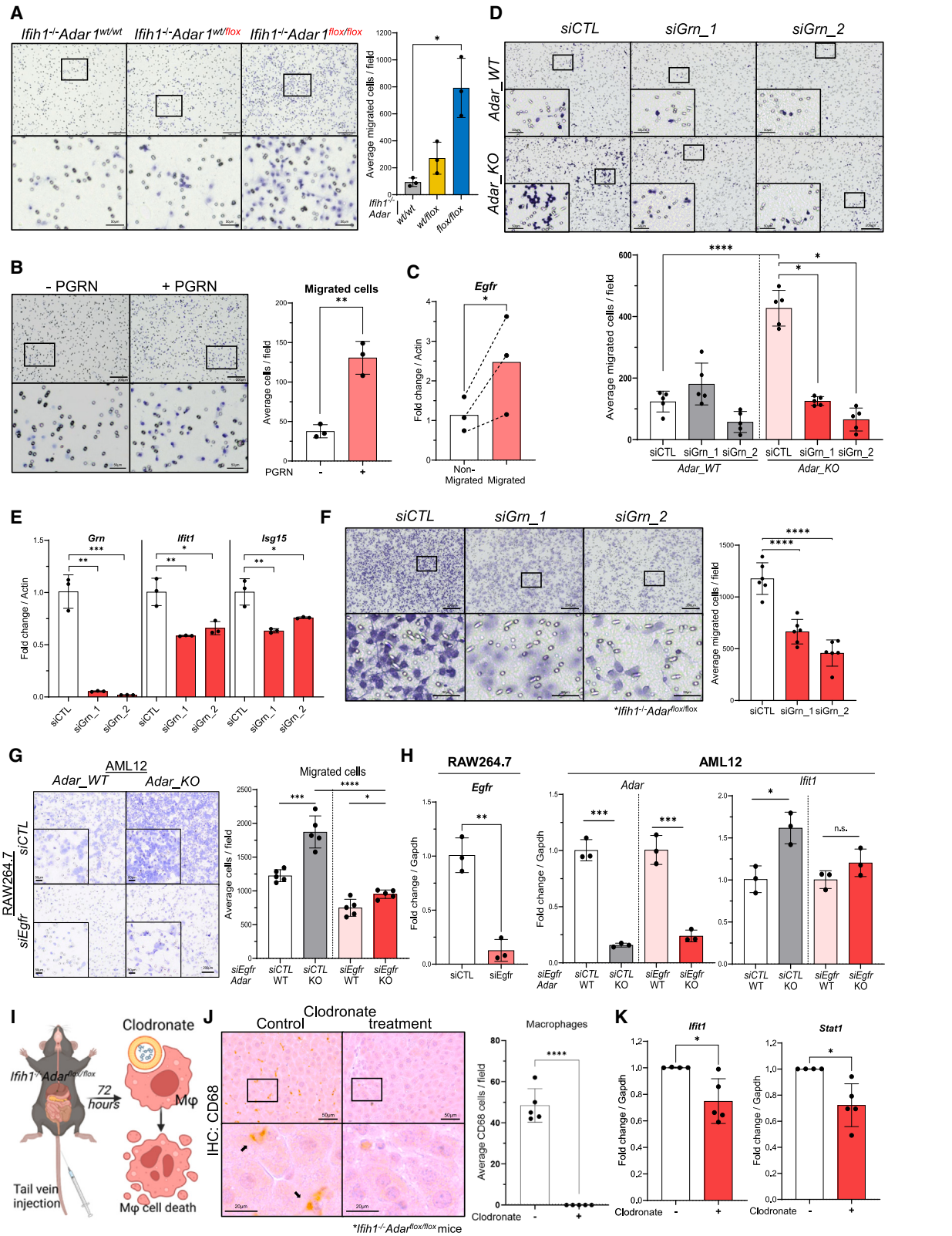

(legend on next page)

PGRN actively recruits EGFR$^+$ macrophages, thereby potentiating hepatic inflammation

To investigate the impact of PGRN on hepatic inflammation in the extracellular environment of dKO livers, we tested whether dKO hepatocytes could induce macrophage recruitment (Figure S12A). Conditioned medium collected from dKO hepatocytes significantly enhanced RAW264.7 murine macrophage migration across a transwell membrane compared to other hepatocyte groups (Figure 5A), suggesting that dKO hepatocytes release factors like PGRN to attract macrophages. Recombinant PGRN alone could induce macrophage migration (Figure 5B), with migrated macrophages showing elevated *Egfr* expression compared to non-migrated ones (Figure 5C).

Depleting *Grn* in ADAR1-deficient AML12 hepatocytes significantly reduced ISG upregulation (Figure 4L) and macrophage migration (Figure 5D). This was confirmed in primary experiments, where silencing *Grn* in primary dKO hepatocytes decreased ISG expression and impaired recruitment of primary bone marrow-derived macrophages (BMDMs) (Figures 5E and 5F).

To further investigate PGRN's effect on hepatic inflammation via recruited macrophages, we collected AML12 hepatocytes at different time points before or after RAW264.7 macrophage migration and analyzed ISG expression (Figure S12B). Our results show a clear association between recruited macrophages and ISG upregulation. Additionally, depleting EGFR significantly reduced macrophage responsiveness to PGRN-induced migration (Figure S12C). Moreover, EGFR-depleted macrophages showed significantly reduced migration in response to conditioned medium from ADAR1-KO AML12 hepatocytes compared to control macrophages (Figure 5G). Consequently, ISG upregulation was substantially attenuated in ADAR1-KO AML12 hepatocytes due to fewer recruited macrophages (Figure 5H). To further investigate the impact of these macrophages on hepatic inflammation *in vivo*, we depleted macrophages in dKO livers using clodronate (Figure 5I). Intravenous clodronate administration effectively depleted macrophages in dKO livers (Figure 5J), thereby dampening hepatic ISG expression (Figure 5K).

Altogether, these findings indicate that PGRN functions as an immune activator in ADAR1-deficient hepatocytes and as a hepatocyte-derived ligand, facilitating hepatocyte-macrophage communication in dKO livers. Released PGRN recruits EGFR$^+$ macrophages, thereby potentiating the inflammatory response.

Depleting GRN weakens the tumor-suppressive effect of ADAR1 depletion by reducing ISG upregulation and macrophage recruitment

Recent evidence connects immune surveillance for infections with mechanisms underlying human diseases like cancer. ADAR1 is now recognized as a key suppressor of innate immune activation, influencing cancer immunity.[10,11] Studies suggest that targeting ADAR1 holds potential therapeutic value, as *Adar* depletion sensitizes B16-F10 melanoma cells to immune checkpoint blockade.[44] Empowered by our mouse studies, we wondered whether high ADAR1 expression in cancer cells contributes to immunosuppression via suppressing PGRN. To test this, we generated *Grn*-KO (Grn^{KO}) and wild-type (Grn^{WT}) B16-F10 melanoma cells. Subsequently, we performed ADAR1 KD and injected these cells subcutaneously into immunocompetent

Figure 5. *Adar* KO hepatocyte-derived PGRN promotes the migration of *Egfr*$^+$ macrophages into the dKO liver and perpetuates hepatic inflammation

(A) Representative images of Transwell migration assays of RAW264.7 macrophages to conditioned medium from the indicated primary cultured hepatocytes. Images below represent magnified views of regions demarcated by a black box (left). A bar plot shows quantification of migrated cells in the indicated conditions (right). Data are represented as mean ± SD for 3 biological replicates.

(B) Representative images of Transwell migration assays of RAW264.7 macrophages to recombinant PGRN-containing medium. Images below represent magnified views of regions demarcated by a black box (left). A bar plot shows quantification of migrated cells in the indicated conditions (right). Data are represented as mean ± SD for 3 biological replicates.

(C) Bar plot showing qPCR of *Egfr* in non-migrated and migrated macrophages described in (B). Data are represented as mean ± SD of 3 biological replicates (a dotted line connects independent experiments). Statistical significance is determined by paired Student's t test (*$p < 0.05$, **$p < 0.01$).

(D) Representative images of Transwell migration assays of RAW264.7 macrophages to conditioned medium from *Adar*_KO or control (*Adar*_WT) AML12 hepatocytes co-transfected with siGrn_1, siGrn_2, or siCTL. Insets represent magnified views of regions demarcated by a black box (top). A bar plot shows quantification of migrated cells in the indicated conditions (bottom). Data are represented as mean ± SD for 2 biological replicates.

(E) Bar chart showing qPCR of *Grn* and the indicated ISGs in primary cultured $Ifih1^{-/-}Adar^{flox/flox}$ hepatocytes transfected with siGrn_1, siGrn_2, or siCTL. Data are represented as mean ± SD for 3 technical replicates.

(F) Representative images of Transwell migration assays of primary murine bone marrow-derived macrophages (BMDMs) to conditioned media described in (E). Images below represent magnified views of regions demarcated by a black box (left). A bar plot shows quantification of migrated BMDMs in the indicated conditions (right). Data are represented as mean ± SD for 2 biological replicates.

(G) Representative images of Transwell migration assays of RAW264.7 macrophages transfected with siEgfr or siCTL in the upper chamber and co-cultured with WT (Adar_WT) or Adar_KO murine AML12 hepatocytes in the bottom well. Inset images represent magnified views of respective images (left). A bar plot shows quantification of migrated cells in the indicated conditions (right). Data are represented as mean ± SD of 5 fields.

(H) Bar plots showing qPCR of Egfr in RAW264.7 macrophages transfected with siEgfr or siCTL (left). Bar plots showing qPCR of *Adar* and *Ifit1* in the co-cultured AML12 Adar_WT or KO hepatocytes (right). Data are represented as mean ± SD of 3 technical replicates.

(I) Schematic showing the experimental setup for macrophage depletion in $Ifih1^{-/-}Adar^{flox/flox}$ livers by tail vein injection of control (Control) or clodronate-containing (Treatment) liposomes to induce macrophage (Mϕ) death. Livers were collected after 72 h.

(J) Representative images of IHC of CD68 macrophages in dKO livers described in (I). Images below represent magnified view of regions demarcated by a black box; black arrows indicate CD68 macrophages (left). A bar plot shows quantification of the number of CD68 macrophages in the indicated conditions (right). Scale bar, 50 μm. Magnified view scale bar, 20 μm.

(K) Bar charts showing qPCR of ISGs in samples described in (J). Data are represented as mean ± SD of ∼4–5 biological replicates.

(A–K) Unless stated otherwise, statistical significance is determined by unpaired, two-tailed Student's t test (*$p < 0.05$, **$p < 0.01$, ***$p < 0.001$, ****$p < 0.0001$).

(A–G) Scale bar, 200 μm. Inset/magnified view scale bar, 50 μm.

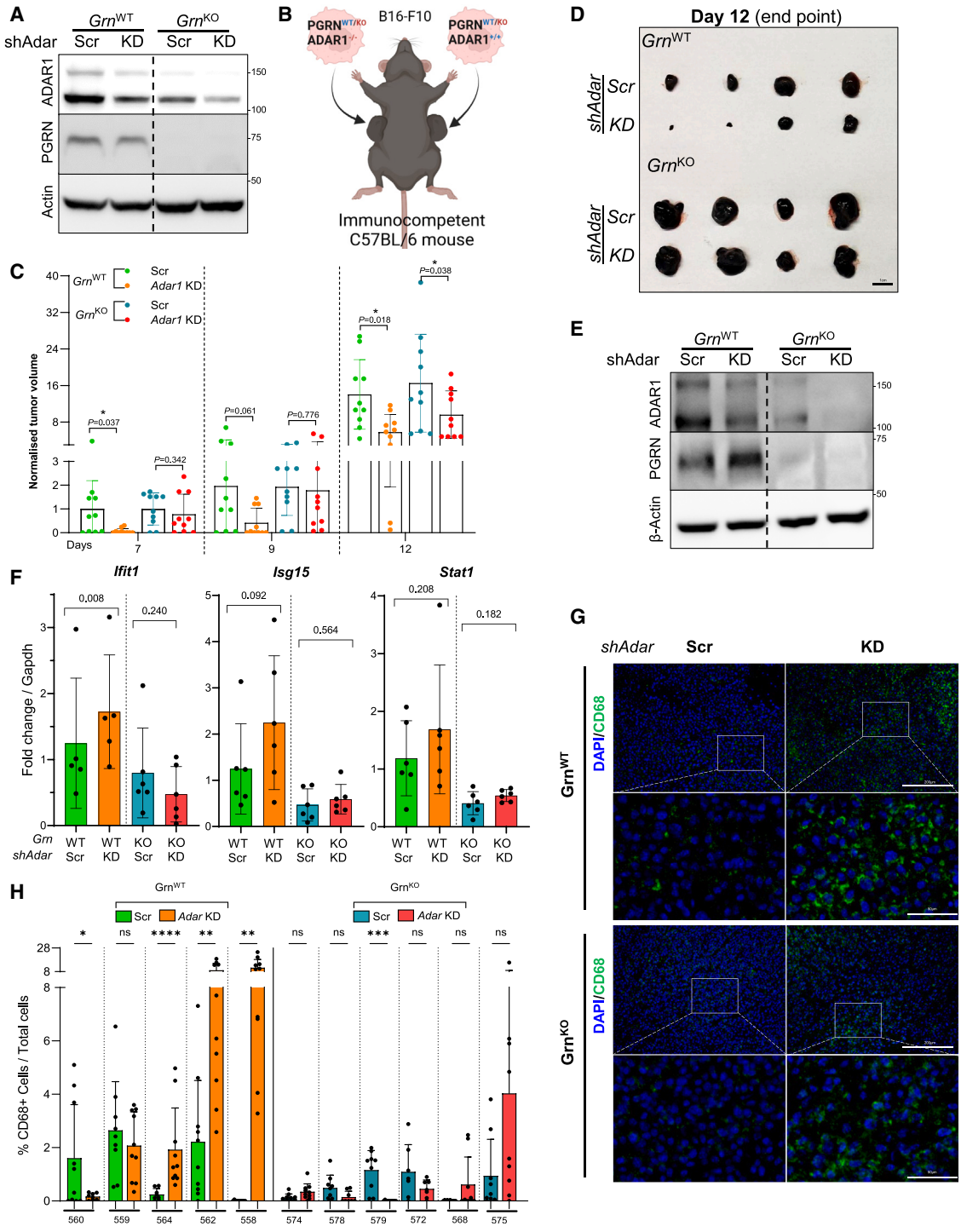

Figure 6. Deletion of *Grn* compromises the tumor-suppressive effect of ADAR1 depletion by reducing ISG upregulation and macrophage recruitment

(A) Western blot of the indicated proteins in *Grn* KO (Grn^{KO}) and WT (Grn^{WT}) B16-F10 melanoma cells with stable lentiviral transduction of shAdar (KD) or control shRNA (Scr).

(B) Schematic showing subcutaneous injection of B16-F10 cells described in (A) into immunocompetent C57BL/6JInv mice.

(C) Bar plots showing normalized volumes of xenograft tumors derived from the indicated groups at days 7, 9, and 12 post injection as described in (B). Data are represented as mean ± SD of 10 tumors per group.

(D) Representative image showing endpoint xenograft tumors derived from the indicated groups. Scale bar, 1 cm.

(legend continued on next page)

mice to assess the impact of ADAR1 depletion, with or without *Grn*, on tumor growth, inflammation, and macrophage infiltration *in vivo* (Figures 6A–6H). Deletion of *Grn* in B16-F10 cells compromised the suppressive effect of ADAR1 KD on tumor growth (Figures 6C and 6D). Upregulation of ISGs and macrophage infiltration was observed in tumors derived from ADAR1 KD Grn^{WT} B16-F10 cells but compromised in tumors derived from the ADAR1 KD Grn^{KO} cells compared to their corresponding Scramble (Scr) control cells (Figures 6E–6H). These results suggest that *Grn* contributes to the tumor-suppressive phenotype observed upon ADAR1 depletion by reducing intrinsic ISG upregulation and limiting extrinsic macrophage recruitment.

ADAR1 contributes to immunosuppression in HCC

Next, we investigated whether ADAR1 depletion could overcome immunosuppression in HCC. We depleted ADAR1 in the murine HCC cell line Hepa1-6, which led to increased PGRN expression and upregulation of ISGs (Figures S13A and S13B). Subsequently, these cells were subcutaneously injected into immunocompetent mice to assess the impact of ADAR1 depletion on tumor growth, inflammation, and macrophage infiltration *in vivo* (Figure 7A). At the endpoint, 4 of 6 tumors derived from ADAR1-depleted Hepa1-6 cells maintained stable *Adar* KD, exhibiting smaller volumes and higher levels of ISGs compared to controls, categorizing them as "immune-active" tumors (Figures 7B and 7C). Conversely, a minority (2 of 6) of tumors showed volumes comparable to controls. Classified as "immune-inactive," these tumors displayed a loss of *Adar* KD and decreased ISG expression (Figures 7B and 7C). Intriguingly, we observed increased PGRN expression overall in tumor cells and a higher number of infiltrating macrophages in *Adar*-KD "immune-active" tumors but not in "immune-inactive" ones (Figure 7D).

We then examined the impact of ADAR1 in HCC immunosuppression in humans. Silencing ADAR1 in the human HCC cell line SNU449 resulted in increased PGRN expression (Figure S13C). Conditioned medium collected from ADAR1-silenced SNU449 cells induced more migrated macrophages than control counterparts (Figures S13D–S13F). We then performed scRNA-seq of primary HCC tumors and matched adjacent non-tumor (NT) samples, yielding a total of 18,885 cells: 7, 545 from adjacent NT tissue and 11,340 from HCC tumors. We identified 13 distinct clusters with 10 annotated cell types (Figures 7E, S13G, and S13H). Consistent with existing knowledge, HCC hepatocytes demonstrated lower ISG expression compared to hepatocytes in adjacent NT tissue (Figure 7F, left). Additionally, we observed lower *GRN* expression in HCC hepatocytes compared to NT hepatocytes (Figure 7F, center), along with markedly reduced *EGFR* expression in macrophages within HCC tumor tissue compared to adjacent NT tissue (Figure 7F, right). These findings suggest suppressed PGRN-EGFR crosstalk signaling in this HCC case.

To further explore the prevalence of suppressed crosstalk mechanisms in HCC, we conducted multiplex immunohistochemistry (mIHC) analysis of several markers, including ADAR1, CD68, PGRN, and EGFR, on a previously constructed HCC tissue microarray (TMA) (STAR Methods).[14] We found that HCC tumors were generally less inflamed compared to their matched NT samples, as evidenced by significantly lower expression of the ISGs *IRF7* and *ISG15* (Figure 7G). Among the tumors, those with higher ADAR1 expression than their matched NT samples ($ADAR1^{high+}$ tumors, $n = 18$) had significantly fewer $EGFR^+/CD68^+$ double-positive macrophages in the tumors compared to the NT counterparts. This association was not observed in HCC tumors, which did not show higher ADAR1 expression than their paired NT samples ($ADAR1^{high-}$ tumors, $n = 5$) (Figure 7H). Although PGRN levels were not significantly lower in $ADAR1^{high+}$ tumors, we noted that 12 of 18 $ADAR1^{high+}$ cases showed either lower or unchanged PGRN levels compared to their matched NT samples (Table S5). Altogether, our findings suggest that when ADAR1 levels are elevated in hepatocytes, the intercellular communication between hepatocytes and macrophages present in the liver might be repressed. This leads to fewer $EGFR^+$ macrophages recruited into the liver, ultimately dampening hepatic immune responses. These findings mechanistically suggest that pre-neoplastic or neoplastic cells may exploit ADAR1-dependent immune tolerance mechanisms to facilitate immune evasion.

DISCUSSION

Nucleic acid-induced immunity and immune tolerance are crucial in human disease. Maintaining a balance between immune reactivity and tolerance is essential to prevent sterile inflammation or immune evasion by malignant cells. Dysregulation of this balance can lead to either overly tolerant or overactive inflammatory responses. Recent research suggests that ADAR1-mediated RNA editing destabilizes endogenously formed dsRNA structures, which are typically immunogenic[45] and can trigger IFN responses via the MDA5/MAVS pathway.[2,3,25] Dysfunction of ADAR1 disrupts type I IFN signaling, contributing to immune disorders and diseases, including cancer.[46] However, little is known about the specific immunostimulatory dsRNA molecules recognized and edited by ADAR1 or the molecular mechanisms underlying ADAR1-RNA recognition and immune sensing following ADAR1 deficiency. Here, we show that removal of MDA5 could rescue liver-specific ADAR1 null mice from embryonic lethality but not

(E) Western blot analysis of the indicated proteins in representative endpoint tumor samples.
(F) Bar plot showing qPCR of ISGs in qualified endpoint tumor samples. Data are represented as mean ± SD of 5–6 tumor pairs per group. The criteria for sample qualification are detailed in STAR Methods.
(G) Representative immunofluorescent staining for $CD68^+$ (green) macrophages and DAPI (blue) in the indicated endpoint tumors. Images below show magnified views of regions indicated by a white box. Scale bar, 200 μm. Magnified view scale bar, 50 μm.
(H) Bar plots showing the percentage of $CD68^+$ macrophages in the indicated tumor pairs. Data are represented as mean ± SD for 7–10 representative fields per tumor.
(C–H) Statistical significance is determined by paired, two-tailed student's t test (*$p < 0.05$, **$p < 0.01$, ***$p < 0.001$, ****$p < 0.0001$).

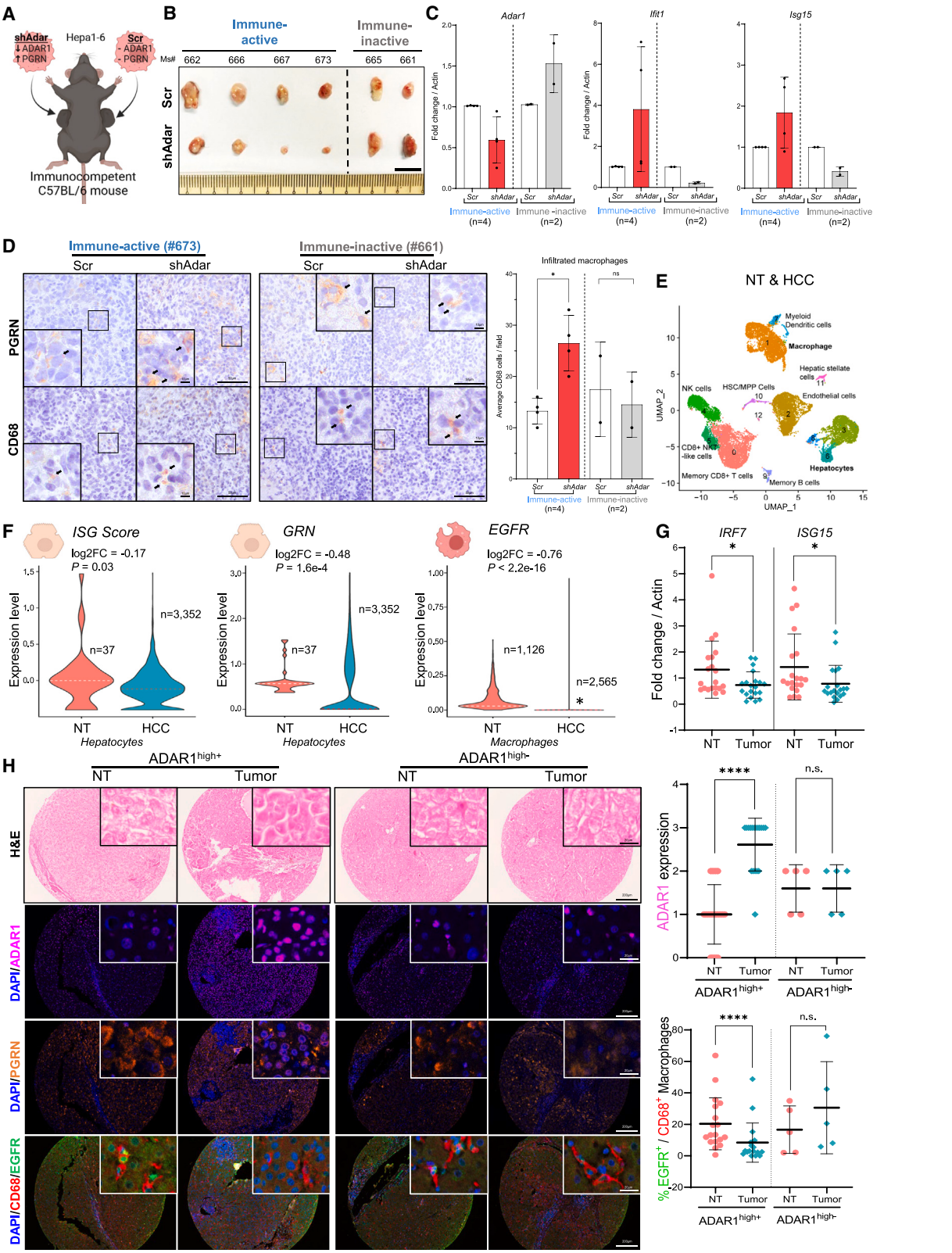

(legend on next page)

hepatic inflammation and dysfunction. Here, we show that removal of MDA5 could rescue liver-specific ADAR1-null mice from embryonic lethality but not hepatic inflammation and dysfunction, as evidenced by histopathological abnormalities and elevated liver damage-related enzymes (Figures 1 and S2H). Previous studies[7,22] using liver-specific conditional *Adar* KO mice in different genetic backgrounds (e.g., Friend leukemia virus B/N [FVB/N] and Sv129) have reported varying outcomes. For instance, Ben-Shoshan et al.[23] found that approximately 10% of hepatocyte-specific *Adar* KO mice (with exons 7–9 deleted [Δexon7–9]) were postnatally viable and survived until the weaning age of 3 weeks, while others exhibited embryonic lethality. These discrepencies could be attributed to differences in mouse background (FVB/N vs. C57BL/6J) or variations in the specific regions of *Adar* that were deleted (Δexon7–9 vs. Δexon12–15).

Through multi-omics profiling of *Ifih1;Adar* dKO livers, we found that dKO hepatocytes underwent intracellular changes, including accumulation of unedited RE-derived dsRNAs, persistent IFN signaling (Figure 1), recruitment of activated macrophages (Figure 2), and aberrant transition into a highly inflammatory hepatocyte population (Cl. 3) (Figure 4). Surprisingly, these changes occurred independent of immune sensing mechanisms involving MAVS/IRF3, PKR/EIF2α, ZBP1/RIP3/MLKL, and OAS/RNAse L (Figures 3 and S8). This aligns with earlier findings showing that concurrent deletion of IRF3 or MAVS failed to fully rescue embryonic lethality following ADAR1 deficiency.[3,4,9] Our findings underscore a current limitation in our understanding of ADAR1's role in exerting self-tolerance to endogenous nucleic acids, particularly regarding tissue specificity of these tolerance mechanisms. Although PKR has been reported to mediate cancer cell death upon ADAR1 ablation in lung and skin cancer cells,[10,11] its role in the liver may differ due to comparatively low expression levels. In contrast, in the skin and intestine, ADAR1 can function as an immune protector by editing Z-RNA species to prevent ZBP1-mediated IFN activation and necroptosis.[31,33,34,47] Mutations in the Zα domain of ADAR1 in mice led to apoptosis in the intestine but not in the liver,[34] indicating tissue-specific effects likely influenced by variable *Zbp1* expression across different tissue types. Here, we observed that most immune-related dKO-Cl.3-SUGs (Figure S8D) were abundant in mouse livers, highlighting their potential roles in liver immunoregulation. Among these genes, PGRN emerged as an immune activator capable of inducing inflammatory responses in hepatocytes, particularly in the absence of ADAR1 (Figures 4B–4E and S10B–S10F). Additionally, we found that activated macrophages were recruited into *Ifih1*;*Adar* dKO livers. Through cell-cell interaction analysis and experimental validation, we showed that PGRN acts as a hepatocyte-derived ligand to recruit activated EGFR$^+$ macrophages into diseased dKO livers, potentially amplifying the inflammatory response (Figures 4, 5, and S12). These findings suggest PGRN as a potential key mediator of liver pathology associated with ADAR1 deficiency. While it is commonly believed that ADAR1 loss leads to the sensing of unedited dsRNAs primarily by the MDA5-MAVS pathway, recent findings from our study and others suggest the involvement of MDA5-independent RNA sensing and immunoregulatory mechanisms.[2,10–12,31,32] Importantly, our study indicates that these mechanisms may depend on cell or tissue type specificity. Moreover, we cannot discount the possibility of unknown editing-independent functions of ADAR1 being essential for ADAR1-mediated immune tolerance *in vivo*. For instance, ADAR1 may shield certain subsets of dsRNAs from RNA sensors or mitigate aberrant immune responses by interacting with other protein(s).

ADAR1's role in suppressing innate immune activation and IFN production has emerged as a key factor in cancer immunity.[10,11] While ADAR1 is necessary under normal conditions for establishing tolerance to self-derived dsRNA and suppressing IFN response post infection to prevent overactivation, these functions can be hijacked by cancer cells to survive despite cytoplasmic dsRNA accumulation. Thus, A-to-I RNA editing by ADAR1 may promote excessive self-tolerance in cancer cells, thwarting IFN activation and cell death. Our study highlights ADAR1 as a crucial regulator of cancer immunity and

Figure 7. ADAR1 and PGRN contribute to immunosuppression in HCC via modulating tumor growth, ISG upregulation, and macrophage recruitment

(A) Schematic showing subcutaneous injection of ADAR1-depleted (shAdar) or scrambled control (Scr) murine HCC Hepa1-6 cells into immunocompetent C57BL/6JInv mice.

(B) Image showing endpoint xenograft tumors derived from the indicated cells described in (A). Scale bar, 1 cm.

(C) Bar charts showing qPCR of *Adar*, *Ifit1*, and *Isg15* in endpoint tumors derived from (A). Data are represented as mean ± SD of 6 biologically independent pairs.

(D) Representative images of IHC detection of PGRN (top) and CD68 (bottom) in the indicated endpoint tumors described in (A). Inset: magnified view of the boxed region; black arrows indicate PGRN$^+$ tumor cells or CD68$^+$ macrophages (left). A bar plot shows quantification of the number of CD68$^+$ macrophages in the indicated endpoint tumors (right). Data are represented as mean ± SD of 6 biologically independent pairs. Scale bar, 50 μm. Inset scale bar, 10 μm.

(E) UMAP visualization of cell clusters and cell type annotation from scRNA-seq of primary HCC tumor and matched adjacent non-tumor (NT) samples.

(F) Violin plot showing expression of ISGs (defined as ISG score) and *GRN* in hepatocytes or *EGFR* in macrophages from NT and HCC tumor samples (a dotted line marks the median value). Statistical significance is determined by Wilcoxon rank-sum test. *P*, *p* value of the Wilcoxon rank-sum test. *, *EGFR* was undetectable in 97.7% of HCC tumor macrophages.

(G) Scatterplots showing qPCR of *IRF7* and *ISG15* in matched pairs of NT and HCC samples (related to H). Data are represented as median ± SD of 20 biological replicates.

(H) Representative multiplexed IHC images of the HCC TMA containing matched pairs of NT and HCC tumor samples stained with H&E, ADAR1 (pink), PGRN (orange), CD68 (red), EGFR (green), and DAPI (blue). Inset: magnified view of respective images. Scale bar, 200 μm. Inset scale bar, 20 μm (left). Scatterplots show expression of ADAR1 in the indicated ADAR1^{high+} and ADAR1^{high-} HCC cases (top right) and the percentage of EGFR$^+$/CD68$^+$ (double-positive) macrophages among all CD68$^+$ macrophages (bottom right), stratified by ADAR1 expression. Data are represented as median ± SD of 23 HCC cases. Scores for expression level of ADAR1 or PGRN are shown in Table S5.

(D, G, and H) Statistical significance was determined by paired Student's t test (*$p < 0.05$, ****$p < 0.0001$).

macrophage infiltration *in vivo* (Figures 6, 7, and S13). Through scRNA-seq and mIHC analysis of primary HCC samples, we found that, in HCC tumors with high ADAR1 levels, intercellular communication between hepatocytes and macrophages via PGRN-EGFR signaling was significantly repressed, resulting in fewer $EGFR^+$ macrophages recruited into the liver, potentially facilitating immune evasion of cancer cells (Figure 7). However, it is important to note that, besides PGRN, other hepatocyte-derived ligands identified may also contribute to these intercellular communications (Figure 4B). Likely, a cumulative effect of multiple interactions, rather than a few isolated ones, work in concert to regulate hepatic inflammation.

The liver is a complex immunological organ known for its high tolerance to harmless self and non-self antigens.[48] It maintains immune homeostasis by tolerating commonly encountered antigens while remaining vigilant to respond to invading pathogens or malignant cells.[49] Our study delves into the mechanisms underlying ADAR1 deficiency-associated liver pathology, shedding light on both intracellular and intercellular processes. Specifically, we uncover the crucial role of intercellular communication between hepatocytes and macrophages via the PGRN-EGFR axis in mediating immunosuppression and immune evasion of HCC cells. This highlights ADAR1 and its downstream crosstalk signaling pathways as potential therapeutic targets for cancers, including HCC.

Limitations of the study

The transgenic mice studied are in the C57BL/6 background, known to exhibit deficits in certain natural killer (NK) cell subpopulations.[50] Notably, our scRNA-seq data did not reveal any distinct NK cell cluster, potentially leading to an underappreciation of their contribution to inflammation in dKO livers due to their lower representation. We nevertheless found that ADAR1 loss is sufficient to induce macrophage-associated hepatic inflammation and dysfunction. The reliance on transcriptomic data limited the insights into signaling events dependent on protein phosphorylation and protein-RNA interactions, limiting information on endogenous self-dsRNA binding to dsRNA sensing proteins in dKO livers, which initiates cell-intrinsic innate immunity. Furthermore, the mechanisms by which ADAR1 regulates GRN expression, how GRN intrinsically activates IFN signaling, and how recruited $EGFR^+$ macrophages perpetuate hepatic inflammation remain to be elucidated.

STAR★METHODS

Detailed methods are provided in the online version of this paper and include the following:

SUPPLEMENTAL INFORMATION

Supplemental information can be found online at https://doi.org/10.1016/j.celrep.2024.114400.

ACKNOWLEDGMENTS

We thank Professor Xin-Yuan Guan from The University of Hong Kong, Hong Kong, China, for providing HCC TMA slides. We acknowledge the Microscopy and Multiplex Assays Core and the Genomics and Data Analytics Core at the Cancer Science Institute of Singapore for conducting mIHC analysis and analysis of DE-REs from bulk RNA-seq data, respectively. Special thanks to Associate Professor Sun Lei from Duke-NUS Medical School, Singapore, for providing *Ifih1*$^{+/-}$ and *Adar*$^{wt/flox}$ mice. We are grateful to Assistant Professor Chen Kaiwen from the National University of Singapore, for providing materials to examine the activation of ZBP1 signaling pathway and BMDMs. This work was supported by National Research Foundation, Singapore; the Singapore Ministry of Education (MOE) under its Research Centers of Excellence initiative; Singapore MOE Academic Research Fund (AcRF) Tier 2 grants (MOE2019 T2-1-083 and MOE2019-T2-2-008); an NMRC Clinician Scientist-Individual Research Grant (MOH-001092-00); the Health and Biomedical Sciences Industry Alignment Fund Pre-Positioning (IAF-PP) (H20C6a0034); and NRF Competitive Research Program (CRP) grants (NRF-CRP26-2021-0001 and NRF-CRP26-2021-0005).

AUTHOR CONTRIBUTIONS

L.C. conceived and supervised the study. L.C. and W.L.G. designed and conducted experiments. X.R. performed most bioinformatics analyses, with assistance from J.X. and O.A. V.T., S.K., and R.D. conducted mouse scRNA macrophage immunophenotyping analyses. V.H.E.N. generated mouse models, conducted phenotyping experiments, and assisted with scRNA-seq. Y.S. aided in primary culture and HCC scRNA-seq experiments. K.H.C.C. generated MDA5ΔN' recombinant protein and performed REMSA and negative-stain EM, with B.W. assisting with data interpretation. L.N., B.Y.L.N., D.J.T.T., J.H., S.J.T., and H.S. provided insightful suggestions. D.Y.Y. assessed histopathological changes in the liver. L.C. and W.L.G. wrote the manuscript, with L.C. editing it.

DECLARATION OF INTERESTS

The authors declare no competing interests.

Received: October 5, 2023
Revised: April 23, 2024
Accepted: June 11, 2024
Published: June 26, 2024

REFERENCES

1. Hartmann, G. (2017). Nucleic Acid Immunity. Adv. Immunol. *133*, 121–169. https://doi.org/10.1016/bs.ai.2016.11.001.

2. Liddicoat, B.J., Piskol, R., Chalk, A.M., Ramaswami, G., Higuchi, M., Hartner, J.C., Li, J.B., Seeburg, P.H., and Walkley, C.R. (2015). RNA editing by ADAR1 prevents MDA5 sensing of endogenous dsRNA as nonself. Science *349*, 1115–1120. https://doi.org/10.1126/science.aac7049.

3. Mannion, N.M., Greenwood, S.M., Young, R., Cox, S., Brindle, J., Read, D., Nellåker, C., Vesely, C., Ponting, C.P., McLaughlin, P.J., et al. (2014). The RNA-editing enzyme ADAR1 controls innate immune responses to RNA. Cell Rep. *9*, 1482–1494. https://doi.org/10.1016/j.celrep.2014.10.041.

4. Pestal, K., Funk, C.C., Snyder, J.M., Price, N.D., Treuting, P.M., and Stetson, D.B. (2015). Isoforms of RNA-Editing Enzyme ADAR1 Independently Control Nucleic Acid Sensor MDA5-Driven Autoimmunity and Multi-organ Development. Immunity *43*, 933–944. https://doi.org/10.1016/j.immuni.2015.11.001.

5. Chen, L. (2023). A-to-I editing prevents self-RNA sensing. Nat. Rev. Mol. Cell Biol. *24*, 85. https://doi.org/10.1038/s41580-022-00540-4.

6. Hartner, J.C., Schmittwolf, C., Kispert, A., Müller, A.M., Higuchi, M., and Seeburg, P.H. (2004). Liver disintegration in the mouse embryo caused by deficiency in the RNA-editing enzyme ADAR1. J. Biol. Chem. *279*, 4894–4902. https://doi.org/10.1074/jbc.M311347200.

7. Wang, G., Wang, H., Singh, S., Zhou, P., Yang, S., Wang, Y., Zhu, Z., Zhang, J., Chen, A., Billiar, T., et al. (2015). ADAR1 prevents liver injury from inflammation and suppresses interferon production in hepatocytes. Am. J. Pathol. *185*, 3224–3237.

8. Chung, H., Calis, J.J.A., Wu, X., Sun, T., Yu, Y., Sarbanes, S.L., Dao Thi, V.L., Shilvock, A.R., Hoffmann, H.H., Rosenberg, B.R., and Rice, C.M. (2018). Human ADAR1 Prevents Endogenous RNA from Triggering Translational Shutdown. Cell *172*, 811–824.e14. https://doi.org/10.1016/j.cell.2017.12.038.

9. Bajad, P., Ebner, F., Amman, F., Szabó, B., Kapoor, U., Manjali, G., Hildebrandt, A., Janisiw, M.P., and Jantsch, M.F. (2020). An internal deletion of ADAR rescued by MAVS deficiency leads to a minute phenotype. Nucleic Acids Res. *48*, 3286–3303. https://doi.org/10.1093/nar/gkaa025.

10. Gannon, H.S., Zou, T., Kiessling, M.K., Gao, G.F., Cai, D., Choi, P.S., Ivan, A.P., Buchumenski, I., Berger, A.C., Goldstein, J.T., et al. (2018). Identification of ADAR1 adenosine deaminase dependency in a subset of cancer cells. Nat. Commun. *9*, 5450–5510.

11. Ishizuka, J.J., Manguso, R.T., Cheruiyot, C.K., Bi, K., Panda, A., Iracheta-Vellve, A., Miller, B.C., Du, P.P., Yates, K.B., Dubrot, J., et al. (2019). Loss of ADAR1 in tumours overcomes resistance to immune checkpoint blockade. Nature *565*, 43–48.

12. Liu, H., Golji, J., Brodeur, L.K., Chung, F.S., Chen, J.T., deBeaumont, R.S., Bullock, C.P., Jones, M.D., Kerr, G., Li, L., et al. (2019). Tumor-derived IFN triggers chronic pathway agonism and sensitivity to ADAR loss. Nat. Med. *25*, 95–102.

13. Chen, L., Li, Y., Lin, C.H., Chan, T.H.M., Chow, R.K.K., Song, Y., Liu, M., Yuan, Y.F., Fu, L., Kong, K.L., et al. (2013). Recoding RNA editing of AZIN1 predisposes to hepatocellular carcinoma. Nat. Med. *19*, 209–216. https://doi.org/10.1038/nm.3043.

14. Chan, T.H.M., Lin, C.H., Qi, L., Fei, J., Li, Y., Yong, K.J., Liu, M., Song, Y., Chow, R.K.K., Ng, V.H.E., et al. (2014). A disrupted RNA editing balance mediated by ADARs (Adenosine DeAminases that act on RNA) in human hepatocellular carcinoma. Gut *63*, 832–843. https://doi.org/10.1136/gutjnl-2012-304037.

15. Fumagalli, D., Gacquer, D., Rothé, F., Lefort, A., Libert, F., Brown, D., Kheddoumi, N., Shlien, A., Konopka, T., Salgado, R., et al. (2015). Principles Governing A-to-I RNA Editing in the Breast Cancer Transcriptome. Cell Rep. *13*, 277–289. https://doi.org/10.1016/j.celrep.2015.09.032.

16. Maas, S., Patt, S., Schrey, M., and Rich, A. (2001). Underediting of glutamate receptor GluR-B mRNA in malignant gliomas. Proc. Natl. Acad. Sci. USA *98*, 14687–14692. https://doi.org/10.1073/pnas.251531398.

17. Jiang, Q., Crews, L.A., Barrett, C.L., Chun, H.J., Court, A.C., Isquith, J.M., Zipeto, M.A., Goff, D.J., Minden, M., Sadarangani, A., et al. (2013). ADAR1 promotes malignant progenitor reprogramming in chronic myeloid leukemia. Proc. Natl. Acad. Sci. USA *110*, 1041–1046. https://doi.org/10.1073/pnas.1213021110.

18. Shigeyasu, K., Okugawa, Y., Toden, S., Miyoshi, J., Toiyama, Y., Nagasaka, T., Takahashi, N., Kusunoki, M., Takayama, T., Yamada, Y., et al. (2018). AZIN1 RNA editing confers cancer stemness and enhances oncogenic potential in colorectal cancer. JCI Insight *3*, e99976. https://doi.org/10.1172/jci.insight.99976.

19. Qin, Y.R., Qiao, J.J., Chan, T.H.M., Zhu, Y.H., Li, F.F., Liu, H., Fei, J., Li, Y., Guan, X.Y., and Chen, L. (2014). Adenosine-to-inosine RNA editing mediated by ADARs in esophageal squamous cell carcinoma. Cancer Res. *74*, 840–851. https://doi.org/10.1158/0008-5472.CAN-13-2545.

20. Roca Suarez, A.A., Testoni, B., Baumert, T.F., and Lupberger, J. (2020). Nucleic Acid-Induced Signaling in Chronic Viral Liver Disease. Front. Immunol. *11*, 624034. https://doi.org/10.3389/fimmu.2020.624034.

21. Hartner, J.C., Walkley, C.R., Lu, J., and Orkin, S.H. (2009). ADAR1 is essential for the maintenance of hematopoiesis and suppression of interferon signaling. Nat. Immunol. *10*, 109–115. https://doi.org/10.1038/ni.1680.

22. Wang, Q., Miyakoda, M., Yang, W., Khillan, J., Stachura, D.L., Weiss, M.J., and Nishikura, K. (2004). Stress-induced apoptosis associated with null mutation of ADAR1 RNA editing deaminase gene. J. Biol. Chem. *279*, 4952–4961. https://doi.org/10.1074/jbc.M310162200.

23. Ben-Shoshan, S.O., Kagan, P., Sultan, M., Barabash, Z., Dor, C., Jacob-Hirsch, J., Harmelin, A., Pappo, O., Marcu-Malina, V., Ben-Ari, Z., et al. (2017). ADAR1 deletion induces NFκB and interferon signaling dependent liver inflammation and fibrosis. RNA Biol. *14*, 587–602. https://doi.org/10.1080/15476286.2016.1203501.

24. Wang, Q., Li, X., Qi, R., and Billiar, T. (2017). RNA editing, ADAR1, and the innate immune response. Genes *8*, 41.

25. Eisenberg, E., and Levanon, E.Y. (2018). A-to-I RNA editing - immune protector and transcriptome diversifier. Nat. Rev. Genet. *19*, 473–490. https://doi.org/10.1038/s41576-018-0006-1.

26. Newman, A.M., Liu, C.L., Green, M.R., Gentles, A.J., Feng, W., Xu, Y., Hoang, C.D., Diehn, M., and Alizadeh, A.A. (2015). Robust enumeration of cell subsets from tissue expression profiles. Nat. Methods *12*, 453–457.

27. Wei, R., He, S., Bai, S., Sei, E., Hu, M., Thompson, A., Chen, K., Krishnamurthy, S., and Navin, N.E. (2022). Spatial charting of single-cell transcriptomes in tissues. Nat. Biotechnol. *40*, 1190–1199.

28. Kwon, D.H., Lee, H., Park, C., Hong, S.H., Hong, S.H., Kim, G.Y., Cha, H.J., Kim, S., Kim, H.S., Hwang, H.J., and Choi, Y.H. (2019). Glutathione induced immune-stimulatory activity by promoting M1-like macrophages polarization via potential ROS scavenging capacity. Antioxidants *8*, 413.

29. Neubert, P., Homann, A., Wendelborn, D., Bär, A.L., Krampert, L., Trum, M., Schröder, A., Ebner, S., Weichselbaum, A., Schatz, V., et al. (2020). NCX1 represents an ionic Na+ sensing mechanism in macrophages. PLoS Biol. *18*, e3000722.

30. Binatti, E., Gerussi, A., Barisani, D., and Invernizzi, P. (2022). The role of macrophages in liver fibrosis: New therapeutic opportunities. Int. J. Mol. Sci. *23*, 6649.

31. Zhang, T., Yin, C., Fedorov, A., Qiao, L., Bao, H., Beknazarov, N., Wang, S., Gautam, A., Williams, R.M., Crawford, J.C., Peri, S., et al. (2022). ADAR1 masks the cancer immunotherapeutic promise of ZBP1-driven necroptosis. Nature *606*, 594–602.

32. Li, Y., Banerjee, S., Goldstein, S.A., Dong, B., Gaughan, C., Rath, S., Donovan, J., Korennykh, A., Silverman, R.H., and Weiss, S.R. (2017). Ribonuclease L mediates the cell-lethal phenotype of double-stranded RNA editing enzyme ADAR1 deficiency in a human cell line. Elife *6*, e25687. https://doi.org/10.7554/eLife.25687.

33. de Reuver, R., Verdonck, S., Dierick, E., Nemegeer, J., Hessmann, E., Ahmad, S., Jans, M., Blancke, G., Van Nieuwerburgh, F., Botzki, A., et al. (2022). ADAR1 prevents autoinflammation by suppressing spontaneous ZBP1 activation. Nature *607*, 784–789.

34. Jiao, H., Wachsmuth, L., Wolf, S., Lohmann, J., Nagata, M., Kaya, G.G., Oikonomou, N., Kondylis, V., Rogg, M., Diebold, M., et al. (2022). ADAR1 averts fatal type I interferon induction by ZBP1. Nature *607*, 776–783.

35. Preston, S.P., Stutz, M.D., Allison, C.C., Nachbur, U., Gouil, Q., Tran, B.M., Duvivier, V., Arandjelovic, P., Cooney, J.P., Mackiewicz, L., et al. (2022). Epigenetic silencing of RIPK3 in hepatocytes prevents MLKL-mediated necroptosis from contributing to liver pathologies. Gastroenterology *163*, 1643–1657.e14.

36. Hu, S.B., Heraud-Farlow, J., Sun, T., Liang, Z., Goradia, A., Taylor, S., Walkley, C.R., and Li, J.B. (2023). ADAR1p150 prevents MDA5 and PKR activation via distinct mechanisms to avert fatal autoinflammation. Mol. Cell *83*, 3869–3884.e7. https://doi.org/10.1016/j.molcel.2023.09.018.

37. Maurano, M., Snyder, J.M., Connelly, C., Henao-Mejia, J., Sidrauski, C., and Stetson, D.B. (2021). Protein kinase R and the integrated stress response drive immunopathology caused by mutations in the RNA deaminase ADAR1. Immunity *54*, 1948–1960.e5. https://doi.org/10.1016/j.immuni.2021.07.001.

38. La Manno, G., Soldatov, R., Zeisel, A., Braun, E., Hochgerner, H., Petukhov, V., Lidschreiber, K., Kastriti, M.E., Lönnerberg, P., Furlan, A., et al. (2018). RNA velocity of single cells. Nature *560*, 494–498.

39. Browaeys, R., Saelens, W., and Saeys, Y. (2020). NicheNet: modeling intercellular communication by linking ligands to target genes. Nat. Methods *17*, 159–162.

40. Cui, Y., Hettinghouse, A., and Liu, C.J. (2019). Progranulin: a conductor of receptors orchestra, a chaperone of lysosomal enzymes and a therapeutic target for multiple diseases. Cytokine Growth Factor Rev. *45*, 53–64.

41. Rhinn, H., Tatton, N., McCaughey, S., Kurnellas, M., and Rosenthal, A. (2022). Progranulin as a therapeutic target in neurodegenerative diseases. Trends Pharmacol. Sci. *43*, 641–652.

42. Hardbower, D.M., Singh, K., Asim, M., Verriere, T.G., Olivares-Villagómez, D., Barry, D.P., Allaman, M.M., Washington, M.K., Peek, R.M., Jr., Piazuelo, M.B., and Wilson, K.T. (2016). EGFR regulates macrophage activation and function in bacterial infection. J. Clin. Invest. *126*, 3296–3312.

43. Wu, B., Peisley, A., Richards, C., Yao, H., Zeng, X., Lin, C., Chu, F., Walz, T., and Hur, S. (2013). Structural basis for dsRNA recognition, filament formation, and antiviral signal activation by MDA5. Cell *152*, 276–289. https://doi.org/10.1016/j.cell.2012.11.048.

44. Ishizuka, J.J., Manguso, R.T., Cheruiyot, C.K., Bi, K., Panda, A., Iracheta-Vellve, A., Miller, B.C., Du, P.P., Yates, K.B., Dubrot, J., et al. (2019). Loss of ADAR1 in tumours overcomes resistance to immune checkpoint blockade. Nature *565*, 43–48. https://doi.org/10.1038/s41586-018-0768-9.

45. Capshew, C.R., Dusenbury, K.L., and Hundley, H.A. (2012). Inverted Alu dsRNA structures do not affect localization but can alter translation efficiency of human mRNAs independent of RNA editing. Nucleic Acids Res. *40*, 8637–8645. https://doi.org/10.1093/nar/gks590.

46. Herbert, A. (2019). ADAR and immune silencing in cancer. Trends Cancer *5*, 272–282.

47. Hubbard, N.W., Ames, J.M., Maurano, M., Chu, L.H., Somfleth, K.Y., Gokhale, N.S., Werner, M., Snyder, J.M., Lichauco, K., Savan, R., et al. (2022). ADAR1 mutation causes ZBP1-dependent immunopathology. Nature *607*, 769–775.

48. Cheng, M.L., Nakib, D., Perciani, C.T., and MacParland, S.A. (2021). The immune niche of the liver. Clin. Sci. *135*, 2445–2466.

49. Robinson, M.W., Harmon, C., and O'Farrelly, C. (2016). Liver immunology and its role in inflammation and homeostasis. Cell. Mol. Immunol. *13*, 267–276.

50. Koehler, H.S., Feng, Y., Mandal, P., and Mocarski, E.S. (2020). Recognizing limits of Z-nucleic acid binding protein (ZBP1/DAI/DLM1) function. FEBS J. *287*, 4362–4369.

51. Stuart, T., Butler, A., Hoffman, P., Hafemeister, C., Papalexi, E., Mauck, W.M., 3rd, Hao, Y., Stoeckius, M., Smibert, P., and Satija, R. (2019). Comprehensive integration of single-cell data. Cell *177*, 1888–1902.e21.

52. Butler, A., Hoffman, P., Smibert, P., Papalexi, E., and Satija, R. (2018). Integrating single-cell transcriptomic data across different conditions, technologies, and species. Nat. Biotechnol. *36*, 411–420.

53. Schneider, C.A., Rasband, W.S., and Eliceiri, K.W. (2012). NIH Image to ImageJ: 25 years of image analysis. Nat. Methods *9*, 671–675.

54. Huang, D.W., Sherman, B.T., and Lempicki, R.A. (2009). Systematic and integrative analysis of large gene lists using DAVID bioinformatics resources. Nat. Protoc. *4*, 44–57.

55. Sherman, B.T., Hao, M., Qiu, J., Jiao, X., Baseler, M.W., Lane, H.C., Imamichi, T., and Chang, W. (2022). DAVID: a web server for functional enrichment analysis and functional annotation of gene lists (2021 update). Nucleic Acids Res. *50*, W216–W221.

56. Chen, E.Y., Tan, C.M., Kou, Y., Duan, Q., Wang, Z., Meirelles, G.V., Clark, N.R., and Ma'ayan, A. (2013). Enrichr: interactive and collaborative HTML5 gene list enrichment analysis tool. BMC Bioinf. *14*, 128–214.

57. Kuleshov, M.V., Jones, M.R., Rouillard, A.D., Fernandez, N.F., Duan, Q., Wang, Z., Koplev, S., Jenkins, S.L., Jagodnik, K.M., Lachmann, A., et al. (2016). Enrichr: a comprehensive gene set enrichment analysis web server 2016 update. Nucleic Acids Res. *44*, W90–W97.

58. Xie, Z., Bailey, A., Kuleshov, M.V., Clarke, D.J.B., Evangelista, J.E., Jenkins, S.L., Lachmann, A., Wojciechowicz, M.L., Kropiwnicki, E., Jagodnik, K.M., et al. (2021). Gene set knowledge discovery with enrichr. Curr. Protoc. *1*, e90.

59. Schwartz, S.L., Park, E.N., Vachon, V.K., Danzy, S., Lowen, A.C., and Conn, G.L. (2020). Human OAS1 activation is highly dependent on both RNA sequence and context of activating RNA motifs. Nucleic Acids Res. *48*, 7520–7531. https://doi.org/10.1093/nar/gkaa513.

60. Li, Y., Banerjee, S., Wang, Y., Goldstein, S.A., Dong, B., Gaughan, C., Silverman, R.H., and Weiss, S.R. (2016). Activation of RNase L is dependent on OAS3 expression during infection with diverse human viruses. Proc. Natl. Acad. Sci. USA *113*, 2241–2246. https://doi.org/10.1073/pnas.1519657113.

61. Yeong, J., Lum, H.Y.J., Teo, C.B., Tan, B.K.J., Chan, Y.H., Tay, R.Y.K., Choo, J.R.E., Jeyasekharan, A.D., Miow, Q.H., Loo, L.H., Yong, W.P., et al. (2022). Choice of PD-L1 immunohistochemistry assay influences clinical eligibility for gastric cancer immunotherapy. Gastric Cancer *25*, 741–750.

62. Qin, Y.R., Qiao, J.J., Chan, T.H.M., Zhu, Y.H., Li, F.F., Liu, H., Fei, J., Li, Y., Guan, X.Y., and Chen, L. (2014). Adenosine-to-inosine RNA editing mediated by ADARs in esophageal squamous cell carcinoma. Cancer Res. *74*, 840–851.

63. Love, M.I., Huber, W., and Anders, S. (2014). Moderated estimation of fold change and dispersion for RNA-seq data with DESeq2. Genome Biol. *15*, 550–621.

64. Hao, Y., Hao, S., Andersen-Nissen, E., Mauck, W.M., 3rd, Zheng, S., Butler, A., Lee, M.J., Wilk, A.J., Darby, C., Zager, M., et al. (2021). Integrated analysis of multimodal single-cell data. Cell *184*, 3573–3587.e29.

65. Shao, X., Liao, J., Lu, X., Xue, R., Ai, N., and Fan, X. (2020). scCATCH: automatic annotation on cell types of clusters from single-cell RNA sequencing data. iScience *23*, 100882.

66. Ianevski, A., Giri, A.K., and Aittokallio, T. (2022). Fully-automated and ultra-fast cell-type identification using specific marker combinations from single-cell transcriptomic data. Nat. Commun. *13*, 1246–1310.

67. Bergen, V., Lange, M., Peidli, S., Wolf, F.A., and Theis, F.J. (2020). Generalizing RNA velocity to transient cell states through dynamical modeling. Nat. Biotechnol. *38*, 1408–1414.

68. Blériot, C., and Ginhoux, F. (2019). Understanding the heterogeneity of resident liver macrophages. Front. Immunol. *10*, 2694.

69. Wolf, A.A., Yáñez, A., Barman, P.K., and Goodridge, H.S. (2019). The ontogeny of monocyte subsets. Front. Immunol. *10*, 1642.

70. Rumianek, A.N., Davies, B., Channon, K.M., Greaves, D.R., and Purvis, G.S.D. (2022). A Human CD68 Promoter-Driven Inducible Cre-Recombinase Mouse Line Allows Specific Targeting of Tissue Resident Macrophages. Front. Immunol. *13*, 918636.

71. Lee, Y.S., Kim, M.H., Yi, H.S., Kim, S.Y., Kim, H.H., Kim, J.H., Yeon, J.E., Byun, K.S., Byun, J.S., and Jeong, W.I. (2018). CX3CR1 differentiates F4/80low monocytes into pro-inflammatory F4/80high macrophages in the liver. Sci. Rep. *8*, 15076.

72. Wu, T., Hu, E., Xu, S., Chen, M., Guo, P., Dai, Z., Feng, T., Zhou, L., Tang, W., Zhan, L., et al. (2021). clusterProfiler 4.0: A universal enrichment tool for interpreting omics data. Innovation *2*, 100141.

STAR★METHODS

KEY RESOURCES TABLE

REAGENT or RESOURCE	SOURCE	IDENTIFIER
Antibodies		
Anti-β-Actin Antibody (C4): sc-47778 [HRP-conjugated]	Santa Cruz	Cat#sc-47778; RRID:AB_626632
Phospho-IRF-3 (Ser396) (4D4G) Rabbit mAb #4947	Cell Signaling Technology	Cat#4947; RRID:AB_823547
IRF-3 (D83B9) Rabbit mAb #4302	Cell Signaling Technology	Cat#4302; RRID:AB_1904036
Phospho-PKR (Thr451) Polyclonal Antibody	Invitrogen	Cat#44-668G; RRID:AB_2533716
PKR Antibody (B-10): sc-6282	Santa Cruz	Cat#sc-6282; RRID:AB_628150
Phospho-eIF2α (Ser51) (D9G8) XP® Rabbit mAb #3398	Cell Signaling Technology	Cat#3398; RRID:AB_2096481
eIF2α (D7D3) XP® Rabbit mAb #5324	Cell Signaling Technology	Cat#5324; RRID:AB_10692650
Phospho-RIP3 (Thr231/Ser232) (E7S1R) Rabbit mAb #91702	Cell Signaling Technology	Cat#91702; RRID:AB_2937060
RIP3 (D4G2A) Rabbit mAb #95702	Cell Signaling Technology	Cat#95702; RRID:AB_2721823
Recombinant Anti-MLKL (phospho S345) antibody [EPR9515(2)] (ab196436)	Abcam	Cat#ab196436; RRID:AB_2687465
MLKL (D6W1K) Rabbit mAb (Mouse Specific)	Cell Signaling Technology	Cat#37705; RRID:AB_2799118
Mouse Progranulin/PGRN Antibody	R&D Systems	Cat#AF2557; RRID:AB_2114504
Anti-rabbit IgG, HRP-linked Antibody #7074	Cell Signaling Technology	Cat#7074P2; RRID:AB_2099233
Anti-mouse IgG, HRP-linked Antibody #7076	Cell Signaling Technology	Cat#7076P2; RRID:AB_330924
Sheep IgG HRP-conjugated Antibody	R&D Systems	Cat#HAF016; RRID:AB_562591
Anti-CD68 antibody (ab125212)	Abcam	Cat#ab125212; RRID:AB_10975465
Anti-CD3 epsilon antibody [SP7]	Abcam	Cat#ab16669; RRID:AB_443425
Anti-ADAR1 Antibody (15.8.6): sc-73408	Santa Cruz	Cat#sc-73408; RRID:AB_2222767
Monoclonal Mouse Anti-Human CD68 (Concentrate) Clone PG-M1	Aligent Dako	Cat#M0876; RRID:AB_2074844
Lamin B1 Polyclonal antibody	Proteintech	Cat#12987-1-AP; RRID:AB_2136290
EGF Receptor Antibody #2232	Cell Signaling Technology	Cat#2232; RRID:AB_331707
Phospho-Stat1 (Tyr701) (D4A7) Rabbit mAb	Cell Signaling Technology	Car#7649T; RRID:AB_10950970
STAT1 Polyclonal antibody	Proteintech	Cat#10144-2-AP; RRID:AB_2286875
Goat anti-Rabbit IgG (H+L) Highly Cross-Adsorbed Secondary Antibody, Alexa Fluor 488	Invitrogen	Cat#A11034; RRID:AB_2576217
Biological samples		
HCC primary tissue	A/Prof Dan Yock Young (Division of Gastroenterology and Hepatology, National University Health System, Singapore)	N/A
HCC TMA	Professor Xin-Yuan Guan (The University of Hong Kong, Hong Kong, China)	N/A
Chemicals, peptides, and recombinant proteins		
Poly(I:C) HMW	Invitrogen	Cat#tlrl-pic
Recombinant Mouse Progranulin Protein, CF	R&D Systems	Cat#2557-PG-050
GILL II HEMATOXYLIN (QT)	Leica	Cat#3801522
EOSIN	Leica	Cat#3801601
Recombinant Mouse TNF-α (carrier-free)	Biolegend	Cat#575206

(*Continued on next page*)

Continued

REAGENT or RESOURCE	SOURCE	IDENTIFIER
AZD5582	Selleck Chemicals	Cat#S7362
Emricasan (IDN-6556)	Selleck Chemicals	Cat#S7775
Critical commercial assays		
10x Genomics Chromium Next GEM Single Cell 3′ kit v3.1 (Dual index)	10x Genomics	Cat#1000268
Visium spatial gene expression slide & reagent kit	10x Genomics	Cat#1000184
Deposited data		
Mouse Bulk RNA sequencing data	GEO	GEO: GSE225175
Mouse Single-cell RNA sequencing data	GEO	GEO: GSE227092
Mouse Spatial Transcriptomics data	GEO	GEO: GSE228195
Human HCC Single-cell RNA sequencing data	GEO	GEO: GSE223204
Experimental models: Cell lines		
AML12 - CRL-2254 - ATCC	ATCC	Cat#ATCC-CRL-2254; RRID:CVCL_0140
SNU449 - ATCC CRL-2234	ATCC	Cat#ATCC CRL-2234; RRID:CVCL_0454
RAW 264.7 - TIB-71 - ATCC	ATCC	Cat#ATCC TIB-71; RRID:CVCL_0493
Hepa 1–6 [Hepa1-6]	ATCC	Cat#CRL-1830; RRID:CVCL_0327
B16-F10	ATCC	Cat#CRL-6475; RRID:CVCL_0159
Experimental models: Organisms/strains		
B6.129-Adartm1Knk/Mmjax	The Jackson Laboratory	MMRRC Strain #034619-JAX RRID:MMRRC_034619-JAX
B6.Cg-Ifih1tm1.1Cln/J	The Jackson Laboratory	Strain #:015812 RRID:IMSR_JAX:015812
B6.Cg-Speer6-ps1Tg(Alb-cre)21Mgn/J	The Jackson Laboratory	Strain #:003574 RRID:IMSR_JAX:003574
C57BL/6JInv	The Jackson Laboratory	Strain #:000664 RRID:IMSR_JAX:000664
Oligonucleotides		
Primers for mouse qPCR data	This study	Table S6
Primers for human qPCR data	This study	Table S6
shRNA sequences for *ADAR1* knock-down	This study	Table S7
shRNA sequences for *Adar* knock-down	This study	Table S7
sgRNA sequences for *Adar* knock-out	This study	Table S7
Software and algorithms		
GraphPad Prism 9	GraphPad	https://www.graphpad.com/scientific-software/prism/
BioRender	BioRender	BioRender.com
R 4.1.2	The R Foundation	https://www.r-project.org
UMAP	Stuart et al.[51]	https://satijalab.org/seurat/
Seurat	Butler et al.[52]	https://github.com/satijalab/seurat
Cellranger 6.1.1	10X Genomics	https://www.10xgenomics.com
Python 3.6.15	Python Software Foundation	https://www.python.org
Anaconda 2019.6	Anaconda	https://www.anaconda.com
Scanpy 1.7.2	PyPI	https://pypi.org
anndata 0.7.6	PyPI	https://pypi.org
numpy 1.19.5	PyPI	https://pypi.org
scipy 1.5.3	PyPI	https://pypi.org
pandas 1.1.5	PyPI	https://pypi.org
NicheNet	Github	https://github.com/saeyslab/nichenetr
RNA Velocity velocyto.py	GitHub	https://github.com/velocyto-team/velocyto.py

(*Continued on next page*)

Continued

REAGENT or RESOURCE	SOURCE	IDENTIFIER
scVelo 0.2.4	GitHub	https://github.com/theislab/scvelo
ImageJ 1.53t	Schneider et al.[53]	https://imagej.nih.gov/ij
DAVID Bioinformatics Resources	Sherman et al., Huang et al.[54,55]	https://david.ncifcrf.gov/home.jsp
Enrichr	Chen et al., Kuleshov et al., Xie et al.[56–58]	https://maayanlab.cloud/Enrichr/
inForm Software 2.6.0	Akoya Biosciences	https://www.akoyabio.com/phenoimager/software/inform-tissue-finder/
Original code for analyses	This Study	https://zenodo.org/records/11274305 (https://doi.org/10.5281/zenodo.11274305)
Others		
ROCHE Collagenase/Dispase	Roche	Cat#10269638001
Invitrogen™ eBioscience™ 1X RBC Lysis Buffer	Invitrogen	Cat#00-4333-57
RQ1 RNase-Free Dnase	Promega	Cat#M6101
DirectPCR Lysis Reagent (Ear)	Viagen	Cat#402-E
Recombinant Proteinase K Solution (20 mg/mL)	Thermo Fisher Scientific	Cat#AM2546
Invitrogen™ Platinum™ Green Hot Start PCR Master Mix (2X)	Thermo Fisher Scientific	Cat#13001012
MiniCollect Complete CAT Serum Separator Clot Activator tubes	Greiner	Cat#450548
SPLInsert™ Hanging	SPL Life Sciences	Cat#35206
Corning™ Falcon™ Cell Culture Inserts	Corning	Cat#353097
Gibco™ HBSS (10X), no calcium, no magnesium, phenol red	Thermo Fisher Scientific	Cat#14180046
Collagenase from Clostridium histolyticum, Type IA	Sigma-Aldrich	Cat#C9891
0.5M EGTA, pH 8.0	1st Base	Cat#CUS-1070
Gibco™ ACK Lysing Buffer	Thermo Fisher Scientific	Cat#A1049201
Percoll®	Sigma-Aldrich	Cat#P1644
Corning® Matrigel® Growth Factor Reduced (GFR) Basement Membrane Matrix	Merck	Cat#CLS356231
SPRIselect for Size Selection	Beckman Coulter	Cat#B23317
Qiagen, Inc. RNeasy Mini Kit	Qiagen	Cat#74106
Advantage® RT-for-PCR Kit	Takara	Cat#639506
GoTaq® qPCR Master Mix	Promega	Cat#A600A
cOmplete™, EDTA-free Protease Inhibitor Cocktail	Roche	Cat#11873580001
PhosSTOP	Roche	Cat#4906845001
Lipofectamine™ 2000 Transfection Reagent	Thermo Fisher Scientific	Cat#11668019
Clearene Solvent	Leica	Cat#3803600
CV Ultra Mounting Media	Leica	Cat#14070936261
VECTASHIELD® Antifade Mounting Medium with DAPI	Vector Laboratories	H-1200-10
Standard Macrophage Depletion Kit (Clodrosome® + Encapsome®)	Encapsula Nano Sciences	SKU# CLD-8901
Paraplast	Leica	39603002
CV Ultra Mounting Media	Leica	cv-ultra-mounting-media
Cover glass Size 22 x 22mm	Fisher Scientific	FIS#12-544-10
Formalin solution, neutral buffered, 10%	Sigma-Aldrich	HT501128
Clearene	Leica	3803600
Target Retrieval Solution, Citrate pH 6.1 (10x)	Dako	S1699
Peroxidase-Blocking Solution, Dako REAL	Dako	S2023

(*Continued on next page*)

Continued

REAGENT or RESOURCE	SOURCE	IDENTIFIER
Protein Block, Serum-Free	Dako	X0909
Antibody Diluent, Background Reducing	Dako	S3022
Goat Anti-Rabbit Immunoglobulins/HRP	Dako	P0448
Poly(I:C) (HMW)	Invivogen	tlrl-pic
Recombinant Mouse IFN-beta (Mammalian) Protein, CF	R&D Systems	12410–1
Ruxolitinib JAK1 and JAK2 Inhibitor - InvitroFit™	Invivogen	#tlrl-rux
Integrated Stress Response inhibitor (ISRIB)	Sigma-Aldrich	SML0843
PKR Inhibitor (PKRi)	Sigma-Aldrich	527450

RESOURCE AVAILABILITY

Lead contact

Further information and requests for resources and reagents should be directed to and will be fulfilled by the lead contact, Leilei Chen (polly_chen@nus.edu.sg).

Materials availability

This study did not generate new unique reagents. Other materials generated in this study are available and will be shared by the lead contact upon request.

Data and code availability

The raw data and processed data for mouse bulk RNA-Seq, mouse scRNA-Seq, mouse spatial transcriptomics, and HCC scRNA-Seq data generated in this study have been deposited in the Gene Expression Omnibus (GEO) under the following accession codes: GEO: GSE225175, GEO: GSE223204, GEO: GSE227092, and GEO: GSE228195.

The original code has been deposited to GitHub (https://github.com/RENXI-NUS/Weiliang_et-al_Adar_SC_MS_manuscript) and Zenodo, https://doi.org/10.5281/zenodo.11274305 (https://zenodo.org/records/11274305) and the links can be found in the key resources table.

Any additional information required to reanalyse the data reported in this manuscript is available from the lead contact upon reasonable request.

EXPERIMENTAL MODEL AND STUDY PARTICIPANT DETAILS

Cultured cell lines

All cell lines were cultured at 37°C in a humidified incubator with 5% CO2 and were obtained from the American Type Culture Collection (ATCC). AML12 cells (ATCC CRL-2254) were cultured in DMEM/F-12 medium (Biowest) supplemented with 10% FBS. RAW264.7 (ATCC TIB-71), SNU449 cells (ATCC CRL-2234), Hepa1-6 cells (CRL-1830), and B16-F10 cells (ATCC CRL-6475) were cultured in DMEM (Gibco) medium supplemented with 10% FBS.

Mice strains

All animal experiments were approved by the Institutional Animal Care and Use Committees of National University of Singapore (NUS; Singapore) with the protocol numbers BR22–00577 and R20-1586. *Adar*^{flox} mutant mice (B6.129-*Adar* ^{tm1Knk}/Mmjax) and *Ifih1*$^{-/-}$ mice (B6.Cg-*Ifih1*$^{tm1.1Cln}$/J) were kindly provided by the laboratory of Associate Professor Sun Lei. Alb-Cre mice (B6.Cg-Speer6-ps1$^{Tg(Alb-cre)21Mgn}$/J) were purchased from the Jackson laboratory and used for breeding. For genotyping, mice ear tips were collected, and genomic DNA was obtained using DirectPCR (Ear) lysis reagent (Viagen #402-E) with 1% Proteinase K (Thermo Fisher Scientific AM2546) according to manufacturer's protocol. PCR was performed using Platinum Green 2X PCR master mix (Invitrogen 13001012). Genotyping of respective mice strains were performed according to genotyping protocols provided by The Jackson Laboratory. All mice used in this study are of B6 background, and all comparisons were performed on age- and gender-matched controls.

HCC tissue samples

All human tissue samples used in this study were approved by the committees for ethics review at the University of Hong Kong, the National University of Singapore (NUS), and the National University Hospital (NUH), Singapore. Written informed consent for all patients were provided for the use of their clinical specimens for medical research. HCC tissue microarray (TMA) samples were kindly

provided by Professor Xin-Yuan Guan from the University of Hong Kong. The HCC TMA slide used in this study contains 58 matched pairs of surgically resected primary HCCs and their adjacent NT liver tissues.[14] One matched pair of fresh HCC and adjacent NT liver tissues used for scRNA-seq was provided by Associate Professor Dan Yock Young from NUS and NUH.

METHOD DETAILS

Cell culture

Generation of ADAR1 knockout (KO) AML12 cells

The *Adar*-KO AML12 cell line was established using lentiviral transduction, followed by puromycin selection. The lentiCRIPSR v2 (Addgene) plasmid containing gRNA sequences targeting *Adar* were used for lentivirus packaging. Single clones of transduced cells were selected for further experiments. Guide RNA sequence is provided in Table S7.

siRNA-mediated KD of Adar, Grn, and Ifih1 in AML12 cells; Egfr in RAW264.7 cells

Dicer-substrate RNAs (DsiRNAs) targeting *Adar* and *Grn* were ordered from Integrated DNA Technologies (IDT). 50nM of Negative Control DsiRNA (NC), mm.Ri.Adar1.13.3 (siAdar1_3), mm.Ri.Grn.13.1 (siGrn_1), mm.Ri.Grn.13.2 (siGrn_2), and mm.Ri.Ifih1.13.2 (siIfih1), were transfected into AML12 cells in 6-well plates with 5μL of Lipofectamine RNAiMax (Thermo Fisher Scientific) per well. siEgfr #mm.Ri.Egfr.13.1 (siEgfr) was transfected into RAW264.7 cells in 6-well plates with 5μL of Lipofectamine RNAiMax (Thermo Fisher Scientific) per well. The cells were collected by scraping 48 h later for downstream experiments, RNA and protein extraction.

Overexpression of Adar in AML12 Adar KD cells

AML12 cells were transfected siRNA targeting *Adar* as described above. Further, the cells were then co-transfected with pLent6 vectors for overexpression of empty vector (EV)), *Adar* p110, or *Adar* p150 by addition of 4ug corresponding vector, using Lipofectamine 2000 (Thermo Fisher Scientific) at a 1:2 ratio in 6-well plates. The cells were collected by scraping 48 h later for RNA and protein extraction.

Generation of stable Adar knockdown (KD) Hepa1-6 cells

The *Adar*-KD stable Hepa1-6 cell line was established using lentiviral transduction, followed by puromycin selection. The pLKO-ADAR1-Scrambled and pLKO-ADAR1-sh2 constructs were used for the lentivirus packaging. Target sequences of each shRNA are provided in Table S7.

Generation of stable Adar knockdown (KD), Grn knockout (KO) B16-F10 cells

The *Grn*-KO B16-F10 cell line was established using lentiviral transduction, followed by puromycin selection. The lentiCRIPSR v2 (Addgene) plasmid containing gRNA sequences targeting *Adar* were used for lentivirus packaging. Single clones of transduced cells were selected for further experiments. Guide RNA sequence is provided in Table S7. Further, *Adar* KD in *Grn* KO B16-F10 cells was performed using pLKO-ADAR1-Scrambled and pLKO-ADAR1-sh2 constructs used for the lentivirus packaging followed by viral transduction. Target sequences of each shRNA are provided in Table S7.

Generation of stable ADAR1 knockdown (KD) SNU449 cells

The *ADAR1*-KD stable SNU449 cell line was established using lentiviral transduction, followed by puromycin selection. The pLKO-ADAR1-Scrambled, pLKO-ADAR1-sh3, and pLKO-ADAR1-sh9 constructs were used for the lentivirus packaging. Target sequences of each shRNA are provided in Table S7.

Treatment of AML12 with HMW Poly(I:C)

AML12 cells were transfected with 2ug/ml High Molecular Weight (HMW) Poly(I:C) (Invivogen) using Lipofectamine 2000 (Thermo Fisher Scientific) at a 1:2 ratio in 6-well plates. The cells were collected by scraping 24 h later for RNA and protein extraction.

Treatment of AML12 with mouse IFNβ

AML12 cells were treated with 1000units/ml, or 10000units/ml Recombinant Mouse IFN-beta (R&D systems) in culture media. The cells were collected by scraping 24 h later for RNA and protein extraction.

HCC tissue sample preparation

For live cell isolation from fresh NT liver and HCC tissue samples, tissues were gently dissociated by mechanical dissection using forceps and scissors in Collagenase/Dispase (Roche 10269638001) over 2–3 h at 37°C. Cells were then passed through a 100μm cell strainer, washed with 30mL of Advanced DMEM/F12 (Gibco 12634-010), and centrifuged at 100g for 5 min at 4°C. Red blood cells were lysed by resuspending cell pellet in RBC lysis buffer (Invitrogen 00-4333-57) for 1 min, diluted with 30mL of cold Advanced DMEM/F12 and centrifuged again. Cells were briefly washed with cold Advanced DMEM/F12 containing 0.5U/ml RQ1 RNase-free DNaseI (Promega M6101), diluted with 30mL of cold Advanced DMEM/F12, and centrifuged again. The live cells were resuspended in cold Advanced DMEM/F12, passed through a 40μm cell strainer to obtain single cell suspensions, and stained with trypan blue cell stain for viability assessment and cell counting prior to scRNA-seq protocol.

Mouse experiments

Mouse liver biomarker measurement

Submandibular blood collection was performed on *Ifih1*$^{-/-}$*Adar*$^{wt/wt,\ wt/flox,\ flox/flox}$*Alb-Cre*$^{+}$ mice every 2 weeks starting from 4 weeks of age to obtain whole blood in MiniCollect Complete CAT Serum Separator Clot Activator tubes (Greiner 450548). Samples were submitted to the Comparative Medicine Diagnostic Lab, NUS, for measurement of liver biomarkers albumin (ALB), Aspartate

Aminotransferase (AST) and Alanine Aminotransferase (ALT). Strong outlier data points exceeding three times of interquartile range variance excluded as outliers.

Two-step collagenase mouse liver perfusion

The inferior vena cava of freshly euthanized mice was punctured with an 18G perfusion needle, and 30mL of 37°C pre-warmed perfusion buffer (1x HBSS) (Gibco 14180046) with 0.5mM EGTA (pH8) (1st Base CUS-1070) was gently perfused through the liver over the course of 5 min until the liver appeared pale. Without disturbing the position of the perfusion needle, 30mL of 37°C pre-warmed digestion buffer (Collagenase 1A in serum-free DMEM) (Sigma-Aldrich C9891) was then perfused through the liver over the course of 5 min until the liver became soft. The liver was then aseptically removed from the mouse into cold DMEM containing 10% FBS. After gross dissection of liver lobes, the lobes were perforated using an 18G needle and dissociated hepatocytes were gently released into the media using a cell scraper. Cells were then passed through a 100μm cell strainer and centrifuged at 50g for 5 min at 4°C. Red blood cells were lysed by resuspending cell pellet in 3mL of Ack Lysing buffer (Gibco A10492-01) for 1 min, diluted with 30mL of cold DMEM containing 10% FBS, and centrifuged again. Finally, cells were resuspended in cold DMEM containing 10% FBS for downstream analyses – droplet-based scRNA-seq, primary cell culture, and protein and RNA extraction.

For scRNA-seq, live cells were isolated using 10% Percoll (Sigma-Aldrich P1644) gradient centrifugation at 200*g* for 15 min at room temperature (RT). The supernatant was aspirated, and remaining cell pellet were briefly washed with cold DMEM containing 10% FBS and 0.5U/ml RQ1 RNase-free DNaseI (Promega M6101), diluted with 30mL of cold DMEM containing 10% FBS, and centrifuged again. The live cells were resuspended in cold DMEM containing 10% FBS, followed by the same steps as described in "HCC tissue sample preparation".

Mouse tail vein administration of clodronate

Standard macrophage depletion kit (Encapsula Nano Science, SKU# CLD-8901) was used to administer Clodronate for macrophage depletion in mouse livers. Control Encapsome, empty liposomes, or treatment Clodrosome, liposomes containing clodronate, was administered intravenously (10μl/g mouse weight) via tail vein injection using a 30G sterile needle. Following injection, mice livers were isolated 72 h post-injection for two-step collagenase perfusion and downstream experiments.

Mouse intraperitoneal administration of ISRIB

Integrated Stress Response inhibitor (ISRIB) (Sigma-Aldrich), or vehicle control (VC), was administered to *Ifih1*$^{-/-}$*Adar*$^{flox/flox}$*AlbCre*$^{+}$ mice via intraperitoneal (*i.p.*) injection at a dose of 5 mg/kg (5% DMSO, 40%PEG300, 5%Tween80, in sterile saline) daily for 10 days. Submandibular blood collection was performed before the first injection (pre-injection baseline, along with control *Ifih1*$^{-/-}$*Adar*$^{wt/wt}$*AlbCre*$^{+}$ mice) and at different timepoints for liver damage marker measurement as described above. At the end of the experiment (day 10), mice were sacrificed for downstream experiments.

Mouse intraperitoneal administration of PKRi

PKR Inhibitor (PKRi) (Sigma-Aldrich), or vehicle control (VC), was administered to *Ifih1*$^{-/-}$*Adar*$^{flox/flox}$*AlbCre*$^{+}$ mice via intraperitoneal (*i.p.*) injection at a dose of 500ug/kg (5% DMSO, 40%PEG300, 5%Tween80, in sterile saline) daily for 10 days. Submandibular blood collection was performed before the first injection (pre-injection baseline, along with control *Ifih1*$^{-/-}$*Adar*$^{wt/wt}$*AlbCre*$^{+}$ mice) and at different timepoints for liver damage marker measurement as described above. At the end of the experiment (day 10), mice were sacrificed for downstream experiments.

Primary mouse hepatocyte culture

Primary hepatocytes obtained from two-step collagenase liver perfusion was seeded on 6-well plates at 7x10^{5} cells per well. Cell culture plates were pre-coated with 1% Matrigel (Merck, CLS356231) in serum-free DMEM/F-12 for 30 min at 37°C. DMEM/F-12 containing 10% FBS was used as cell culture medium. Conditioned media from primary cultured cells was collected 24 h after seeding, centrifuged at 4,000rpm for 10 min at 4°C before passing through 0.2μm filters and stored at −80°C. For KD of *Grn* in *Ifih1*$^{-/-}$*Adar*$^{flox/flox}$*Alb-Cre*$^{+}$ primary cultured hepatocytes, siRNA targeting mouse *Grn* was transfected as previously described.

Primary mouse hepatocyte treatment with ISRIB and PKRi

Primary hepatocytes were obtained as described above. ISRIB [100nM], or PKRi [1uM] was added to the culture media for 24 h, before collection of cells for downstream experiments.

Primary mouse bone marrow derived macrophage (BMDM) culture

Bone marrow progenitors from mouse femur and tibia were differentiated in high glucose DMEM supplemented with 20% L929 conditioned media as a source of M-CSF, 10% heat-inactivated FBS, 1% HEPES, 1% non-essential amino acid (NEAA) and 1% GlutaMAX for days. Day 6 fully differentiated BMDMs were frozen down and kept at −180°C. Day 6–9 BMDMs were used for experiments. BMDMs were kindly provided by the lab of Assistant Professor Chen Kaiwen.

Trans-well migration assay

For *trans*-well migration assays, we used 24-well (Corning 353097) or 6-well (SPL 35206) transwell inserts with an 8 μm pore size and plates according to manufacturer's instructions. Briefly, for quantifying migrated macrophages, 1.0×10^{5} RAW264.7 macrophages, or 1.0×10^{5} primary BMDMs, were seeded in 300μL of serum-free DMEM in the 24-well *trans*-well inserts and 700μL of control serum-free DMEM, or serum-free DMEM containing recombinant mouse PGRN (R&D Biotech 2557-PG), or conditioned media from primary culture cells, or conditioned media collected after 24 h from 1×10^{6} *Adar*-KD; *Grn*-KD AML12 seeded cells, or conditioned media collected after 24 h from 2×10^{6} *Ifih1*$^{-/-}$*Adar*$^{flox/flox}$*Alb-Cre*$^{+}$ primary culture hepatocytes, or conditioned media collected after 24 h from 1×10^{6} ADAR1-KD SNU449 seeded cells was added into the wells of plates. To collect non-migrated and migrated

macrophages, a total of 1×10^6 RAW264.7 macrophages were seeded in 1mL of serum-free DMEM in the 6-well inserts, and 2mL of control serum-free DMEM or serum-free DMEM containing recombinant mouse PGRN (R&D Biotech 2557-PG) was added into the wells. For quantification, after 16 h of incubation, the inserts were washed in 1x PBS and cells on the top of insert were scrapped off using sterile cotton buds 3 times, followed by fixation in methanol for 20 min at RT. Cells were then stained for 1 h with 0.2% Crystal violet stain. Membranes of *trans*-well inserts were then mounted on slides using mounting media before imaging using EVOS7000 microscope. For each biological replicate, two or more technical replicates were performed. Five randomly selected fields at the center of each *trans*-well membrane were used for counting of migrated cells, followed by quantification using ImageJ.[53]

To extract total RNA from migrated cells, after removing unmigrated cells from top of the insert as mentioned above, migrated cells on the bottom were dislodged by directly placing the insert in Trizol reagent. As for RNA extraction from unmigrated cells, after removing migrated cells from bottom of the insert by scraping, Trizol reagent was added to the insert. Total RNA was then extracted from migrated or unmigrated cells using Trizol-Chloroform method.

For *trans*-well migration assays involving coculture of AML12 cells, RAW264.7 macrophages were seeded in the top chamber as described above, and 0.5×10^6 AML12 cells were seeded in the bottom well.

In vivo allograft assays

C57BL/6JInv (The Jackson Laboratory, Strain #:000664, RRID:IMSR_JAX:000664) mice were maintained in pathogen-free (SPF) facility in NUS Comparative Medicine Department. Less than five mice with same sex were housed in a cage at 20–25°C and 50% humidity with a 12 h light/dark cycle. For *in vivo* HCC allograft assay, 5×10^6 stable *Adar* KD Hepa1-6 cells were subcutaneously injected into the left (Scrambled control) and right flank (*Adar* KD) of 8-week-old female C57BL/6JInv mice ($n = 6$ mice). All animal experiments were approved by and performed in accordance with the Institutional Animal Care and Use Committees (IACUC) of National University of Singapore. All tumors were harvested 7 days after injection. Harvested tumors were used for FFPE tissue sections, and RNA extraction for downstream experiments.

For *in vivo* melanoma allograft assay, 1×10^6 stable *Adar* KD, *Grn* KO B16-F10 cells were subcutaneously injected into the left (*Adar* Scrambled control) and right flank (*Adar* KD) of 8-week-old female C57BL/6JInv mice (*Grn* WT, $n = 10$ mice; *Grn* KO, $n = 10$ mice). All animal experiments were approved by and performed in accordance with the Institutional Animal Care and Use Committees (IACUC) of National University of Singapore. All tumors were harvested 12 days after injection. Tumor volumes are normalized to the average volume of tumors derived from Grn^{WT} B16-F10 cells transduced with Scr, at day 7 post injection. Harvested tumors were used for FFPE tissue sections, and protein and RNA extraction for downstream experiments. Due to tumor size and processing of sample for multiple experiments, drop-out criteria for exclusion of tumor pairs in downstream experiments or analysis are as follows. Tumors deemed too small for FFPE processing or protein extraction were only processed for RNA extraction. All tumors underwent RNA extraction. Tumors deemed too small for FFPE processing were processed for protein and RNA extraction. Protein: tumors with no or low protein concentration were excluded from analysis. RNA: tumor pairs with one or both tumors that (A) RNA could not be extracted, (B) extreme RNA concentration difference between paired samples (>5-fold), (C) extreme difference in house keeping gene expression (>3-fold), 4) one qPCR strong outlier data point exceeded Quartile3 (Q3) + 3x Interquartile range (IQR), were not included in analysis. FFPE: all tumor pairs that successfully underwent FFPE processing were included.

RT-qPCR

Pelleted cells were resuspended in 1mL of Trizol reagent and left on ice for 30 min. A total of 200μL of Chloroform was added and the sample was vortexed prior to being centrifuged for 10 min at 13,000 rpm at 4°C. The supernatant was collected, and isopropanol was added in 1:1 ratio. The precipitated RNA was added to RNeasy columns (Qiagen 74106). The RNeasy RNA extraction process was performed according to manufacturer's protocol with in-column DNaseI treatment and RNA was eluted in RNase-free water. RNA concentration was quantified using Nanodrop. A total of 1,000 ng RNA was used for reverse transcription using Advantage RT-for-PCR Kit (Takara #639506). Each biological replicate qPCR experiment was performed in technical triplicates using GoTaq qPCR master mix (Promega A600A) in a QuantStudio 5 Real-Time PCR system (Applied Biosystems, A34322). Fold change was calculated by $2^{-\Delta\Delta Ct_{sample}}$. $\Delta Ct = Ct_{target} - Ct_{actin;}$ $\Delta\Delta Ct = \Delta Ct_{sample} - average\Delta Ct_{control}$. Primer sequences used for qPCR are provided in Table S6.

Western blot

Pelleted cells were resuspended in RIPA buffer (Sigma) with 1x cOmplete Protease inhibitor (Roche 05056489001) and 1x PhosSTOP phosphatase inhibitor (Roche 04906837001). Cells were lysed on ice for 40 min and centrifuged for 15 min at 13,000 rpm at 4°C. The lysate supernatant was collected.

Protein concentration was quantified using Bradford assay (Bio-Rad). Lysates were denatured in 2x Laemmli buffer (Sigma S3401-10VL) at 95°C for 10 min prior to SDS PAGE. A total of 25μg (total lysates of cell lines) or 20∼100μg (total lysates of perfused mouse livers) were loaded into 8% or 10% polyacrylamide gels for SDS-PAGE, followed by transferred onto polyvinylidene difluoride membranes (Millipore) and incubated with primary antibodies overnight at 4°C and secondary antibodies (1:10,000 dilution) at RT for 1 h. Finally, enhanced chemiluminescence (ECL) (Thermo Fisher, 32106) or West Femto (Thermo Fisher, 34096) was used to visualize the blots using Chemidoc imaging system (Bio-rad). Antibodies used in this study include: anti-β-Actin (1:5,000, Santa Cruz, sc-47778), anti-phospho-IRF3 (1:1,000, CST, 4947), anti-IRF3 (1:1,000, CST, 4302S), anti-phospho-PKR (1:1000, Invitrogen, 44-668G),

anti-PKR (1:1,000, Santa Cruz, sc-6282), anti-phospho-eIF2α (1:1,000, CST, 3398), anti-eIF2α (1:1,000, CST, 5324), anti-phospho-RIP3 (1:1,000, CST, 91702), anti-RIP3 (1:1000, CST, 95702S), anti-phospho-MLKL (1:1,000, Abcam, ab196436), anti-MLKL (1:1,000, CST,37705), anti-PGRN (1:400, R&D systems, AF2557), anti-ADAR1 (1:1,000, Abcam, ab88574), anti-PGRN (1:1000, Sigma-Aldrich, 1:1000), anti-rabbit IgG (1:10,000, CST, 7074P2), anti-mouse IgG (1:10,000, CST, 7076P2), anti-Sheep IgG (1:10,000, R&D systems, HAF016). Unless stated, β-Actin was used as a loading control. Quantification of signal intensity was performed using ImageJ[53] according to protocol described in https://www.yorku.ca/yisheng/Internal/Protocols/ImageJ.pdf.

(1) *Treatment of AML12 cells*. AML12 murine hepatocytes were transfected with 2μg/ml high molecular weight (HMW) Poly(I:C) (Invivogen #tlrl-pic), together with 4μg/ml Lipofectamine 2000 (Invitrogen 11668019) in Opti-MEM medium (Gibco 31985070) for 6 h before harvesting cells for protein extraction. Cell lysates of untreated and treated AML cells were loaded in the same gel as test samples.
(2) *Treatment of BMDMs.* Mouse bone marrow derived macrophages (BMDMS) were treated with 100 ng/mL TNFα (Biolegend, 575206), 1μM AZD5582 (Selleck Chemicals S7362) and 10 μM Emricasan (Selleck Chemicals S7775) for 6 h before harvesting cells for protein extraction. Cell lysates of untreated and treated BMDMs were loaded in the same gel as test samples.

Activation of OAS/RNase L

Total RNA was extracted from cells obtained from perfused mouse livers and RNA was resolved using RNA 6000 Nano bioanalyzer kit (Agilent). RNA integrity was assessed via observing rRNA cleavage as a readout for OAS/RNase L pathway activation.[59,60]

Histology

H&E staining

Hematoxylin and Eosin (H&E) staining was performed on fixed paraffin embedded (FFPE) liver tissue samples. Briefly, tissue samples were fixed in 10% neutral-buffered formalin overnight at room temperature before embedding in paraffin. Paraffin blocks were sectioned at 5 μm thickness. FFPE slides were deparaffinized with xylene substitute Clearene (Leica 3803600) thrice, followed by rehydration with decreasing ethanol concentrations (2 × 100% absolute ethanol, 90% ethanol, 80% ethanol, and 70% ethanol) (5 min each step). Slides were then stained with hematoxylin (Leica 3801522) for 1 min, acid-alcohol for 1 min, and eosin (Leica 3801601) for 1 min, with washes in running water for 1 min between each step. Finally, slides were dehydrated in increased ethanol concentrations (70% ethanol, 80% ethanol, 90% ethanol, and 2 × 100% absolute ethanol), followed by 2 x Clearene. Slides were mounted with CV Ultra mounting medium (Leica 14070936261) and coverslips applied prior to imaging on EVOS M7000 imaging system.

Immunohistochemistry (IHC) detection of macrophages and lymphocytes in mouse liver

Mouse livers collected were fixed in 10% neutral buffered formalin (NBF) (Sigma-Aldrich, HT501128) overnight at RT before transferring to cold 70% ethanol. Tissue processing was performed by incubation of tissues in 70% ethanol, 80% ethanol, 90% ethanol, two changes of 100% ethanol, two changes of Clearene (Leica, 3803600) and two changes of paraffin wax Paraplast (Leica, 39603002) for 1 h each at RT before embedding. FFPE blocks were sectioned at 5μm thickness using a microtome and slides incubated at 37°C overnight. Slides were deparaffinized in two changes of Clearene, two changes of 100% ethanol, 90% ethanol, 80% ethanol, 70% ethanol, and water. Antigen retrieval (Dako, S1699) was performed, and slides were washed in water before peroxidase quenching for 30 min at RT (Dako, S2023) followed by washing. Blocking was performed for 1 h at RT (Dako, X0909) before applying primary antibodies diluted 1:50 in antibody diluent (Dako, S3022) overnight at 4°C. Slides were washed in 0.1% TBST 3 times for 15 min each before applying secondary antibodies (Dako, P0448) followed by washing in 0.1% TBST 3 times for 15 min each. Slides were counterstained in hematoxylin (Leica 3801522) for 1 min, washed for 1 min in water, acid-alcohol for 1 min, washed for 1 min in water, before rehydration through alcohol series ending in Clearene. Mounting CV mounting media (Leica, cv-ultra-mounting-media). Antibodies used in this study include: anti-CD68 (1:250, Abcam, ab125212). Quantification of $CD68^+$ macrophages was performed by imaging of 5 randomly selected fields of view followed by counting using ImageJ.[53] No-primary antibody controls were included.

Immunocytochemistry (ICC) of primary hepatocytes

Primary hepatocytes were isolated from transgenic mice via two-step collagenase perfusion and 200,000 live cells were seeded on sterile glass coverslips (Fisher Scientific, FIS#12-544-10) pre-coated with 1% Matrigel (Merck, CLS356231) in serum-free DMEM/F-12 for 30 min at 37°C in 6-well cell culture plates. After allowing to attach overnight, plates were first washed with PBS before fixing with cold methanol for 30 min and washed 3 times in 0.05% PBST for 5 min each. Blocking was performed using filtered 3% BSA in 0.05% PBST for 1 h at RT. Primary antibodies were diluted in filtered 3% BSA in 0.05% PBST and applied for overnight incubation at 4°C. Wells were washed 3 times in 0.05% PBST for 5 min each before secondary antibodies were applied for 1 h at RT. Wells were then washed 3 times in 0.05% PBST for 5 min each before removing coverslips and mounting with Vectashield antifade mounting media containing DAPI (Vector laboratories, H-1200-10). Antibodies used in this study include: anti-dsRNA [J2] (1:1,000, SCICONS, 1001050), anti-PGRN (1:1,000, Sigma, HPA008763), anti-rabbit IgG Rhodamine Red-X (1:1,000, Invitrogen, R6394), anti-mouse IgG Alexa Fluor 488 (1:1,000, Invitrogen, A11029). No-primary antibody controls were included. For quantification of signal intensities, 4 random image fields per condition were obtained, followed by measurement of integrated density of each cell using ImageJ.[53]

OPAL multiplexed IHC staining and scoring method

FFPE tissue slides were submitted to the Microscopy and Multiplex Assays Core (CSI, NUS) for OPAL multiplex IHC staining using Opal Multiplex fIHC kit (Akoya Biosciences, California), as described previously.[61] Briefly, FFPE slides were deparaffinized and re-hydrated, followed by antigen retrieval using a Leica Bond Max autostainer (Leica Biosystems, Melbourne). Slides were then treated with endogenous peroxidases (Leica Biosystems, Newcastle) and incubated with primary antibodies, HRP-conjugated secondary antibodies, and Opal fluorophore-conjugated tyramide signal amplification (TSA) (1:100, Akoya Biosciences, California). Washing was performed with wash buffer (BOND Wash Solution 10 x Concentrate) between steps. Heat-induced antigen retrieval was performed to strip the slides before repeating abovementioned processes for all target staining. Finally, slides were subjected to spectral DAPI (1:10, Akoya Biosciences, California) labeling before mounting using ProLong Diamond Anti-fade Mountant (Molecular Probes, Life Technologies, USA). Antibodies used included anti-mouse CD68 (1:1,000, Abcam, ab125212), anti-human ADAR1 (1:1,000, Santa Cruz, sc-73408), anti-human CD68 (1:100, DAKO #M0876), anti-human EGFR (1:100, CST, #2232). Imaging of stained slides was performed sing Vectra 2 intelligent slide analysis system (Caliper LifeSciences) and analysis was performed using inForm Software (version 2.6.0; Akoya Biosciences). Briefly, inForm Software 2.6.0 (Akoya Biosciences) was used to unmix signals, perform cell segmentation, and phenotype cells based on trained algorithms.

For patient HCC samples, a TMA comprising 58 surgically resected primary HCCs and their matched NT liver tissues was stained.[14] Informative mIHC results were obtained from 23 matched pairs of HCC and adjacent NT liver tissues, excluding samples that were lost, improperly stained, or had insufficient cells for analysis. Paired NT and tumor slides were processed and image intensities scaled to view across pairs. For analysis of $CD68^+$ and EGFR+ co-expression, the phenotype function of inForm software was trained across individual pairs.

To score the signal intensities of ADAR1 and PGRN, immunoreactivity was scored as negative (0; total absence of staining), weak expression (1; faint staining in <50%, or moderate staining in <25% of cells), moderate expression (2; moderate staining in > = 25% to <75%, or strong staining in <25% of cells), and strong expression (3; moderate staining in > = 75%, or strong staining in > = 25% of cells), as described previously.[62]

For $CD68^+$ macrophage detection in allografted B16-F10 tumors, the grading function of inForm software was used to determine percentage of CD68 positive cells in each field. Strong outlier data points exceeding Quartile3 (Q3) + 3x Interquartile range (IQR), were not included in analysis.

Detection of MDA5-dsRNA interaction by RNA electrophoretic mobility shift assay (REMSA)

MDA5ΔN' expression and purification - The constructed plasmids were transformed into BL21(DE3) (NEB) and grown in Miller's LB broth (Biobasic, SD7002) at 37°C until an OD600 of about 0.6–0.8, then the temperature was lowered to 16°C, and induced with 0.5mM IPTG overnight. Expressed cells were harvested and resuspended with lysis buffer (20mM Tris-HCl, pH 8.0, 300mM NaCl, 20mM imidazole, and 10% glycerol. Cells were then lysed by Emulsiflex-C3 and centrifuged at a speed of 30,000×g (Avanti JXN series, Beckman Coulter) for 20 min at 4°C to separate supernatant and pellet. The supernatant was passed through a pre-equilibrated column containing Ni-NTA agarose beads (ThermoFisher Scientific, R90101) by gravitation flow. The column was then washed with lysis buffer containing 20mM imidazole to remove nonspecific binding proteins. His-NusA-tagged proteins were eluted with increase gradient of imidazole till 300mM in the elution buffer. Elution containing the His-NusA-MDA5ΔN' was added with HRV 3C protease and dialyzed in buffer containing 20mM Tris pH7.5, 50mM NaCl and 10mM DTT overnight at 4°C. For heparin purification of NusA-tag removed MDA5ΔN', HiTrap Heparin HP 5mL (Cytiva, 17040701) in Buffer A (20mM Tris pH 7.5, 50mM NaCl, 5% glycerol) and Buffer B (20mM Tris pH7.5, 1M NaCl, 5% (v/v) glycerol) was used. Fractions containing MDA5ΔN' with measured ratio of 260/280 ideally lesser than 0.8 was further purified to homogeneity with Superdex 200 Increase 10/300 GL (Cytiva, 28990944) in SEC buffer (20 mM Tris pH 7.5, 150 mM NaCl, 5% (v/v) glycerol). Purified MDA5ΔN' protein was immediately used for assay or stored in 4°C for no longer than 5 days.

Synthesis of BRI3BP dsRNA probes - BRI3BP dsRNA was synthesized using T7 RiboMAX Express Large Scale RNA Production System (Promega) and linearized plasmid containing BRI3BP 3′UTR inverted Alus was used as template. *In vitro* transcribed dsRNA was subsequently purified using RNeasy kit (Qiagen) followed by gel purification. BRI3BP dsRNA probes were validated in-house to be recognized and bound by MDA5.

REMSA - 10nM of dsRNA (*in vitro* synthesized BRI3BP probes) was mixed with the indicated amount of MDA5ΔN' in reaction buffer (20mM Tris, pH 7.5, 150mM NaCl, 1.5mM MgCl2, and 2mM DTT). The mixture was incubated at RT for 10 min and were analyzed on NuPAGE 4 to 12%, Bis-Tris, 1.0–1.5mm, Mini Protein Gels (ThermoFisher Scientific, NP0321BOX). Gels was stained with SYBR gold nucleic acid gel stain, according to the manufacturer protocol.

Bulk RNA-seq and scRNA-seq

Two batches of perfused mouse liver samples were sent for scRNA-seq and bulk RNA-seq, and the data shown are from one batch of mice. Nonetheless, changes observed in the presented dataset are consistent with the other batch.

(1) *Bulk RNA-seq*. Total RNA was extracted and subjected to rRNA depletion. RNA quality was determined using an Agilent 2100 Bioanalyzer. Only samples with RNA integrity number (RIN) exceeding 8 were sent for library construction and sequencing by Novogene using the NEBNext UltraTM RNA Library Prep Kit for Illumina (NEB, USA) according to manufacturer's protocol with

index codes added. Briefly, ribosome RNA was depleted, and fragmentation performed using divalent cations under elevated temperature in NEBNext First Strand Synthesis Reaction Buffer(5x). First strand cDNA was synthesized using random hexamer primer and M-MuLV Reverse Transcriptase (RNase H-) before second strand cDNA was synthesized using DNA Polymerase I and RNase H with the incorporation of dUTP. Overhangs were converted to blunt ends using exonuclease/polymerase activities before adenylation of 3′ ends and ligation of NEBNext adaptor within hairpin loop for hybridization. Size selection of purified library fragments were performed using AMPure XP system (Beckman Coulter, Beverly, USA) to digest second strand with size-selected, adaptor ligated cDNA at 37°C for 15 min followed by 5 min at 95°C before PCR. Library amplification was performed using Phusion High-Fidelity DNA polymerase, Universal PCR primers and Index Primer. The libraries were then sequenced on the Illumina HiSeq X platform.

(2) *Droplet-based scRNA-seq*. 10x Genomics Chromium Next GEM Single Cell 3′ kit v3.1 (Dual index) (10x Genomics, 1000268) was used according to manufacturer's protocol. Briefly, cell suspensions were loaded onto Chromium Next GEM Chip G for Gel-in-emulsion (GEM) generation at concentrations targeting 10,000 cells recovery per sample along with barcoded Single Cell 3′ V3.1 gel beads for poly-adenylated mRNA capture and partitioning oil. Only cell suspensions with more than 70% viability (determined by trypan blue stain) were used. Following GEM generation, partitioned cells were lysed and captured RNA were reverse transcribed to first-strand cDNA. GEMs were then broken and Dynabeads MyONE SILANE (10x, 2000048) were used for cleanup before full-length, barcoded cDNA was PCR amplified for library construction. Library preparation was performed according to manufacturer's protocol (CG000315 Rev A). This involved enzymatic fragmentation and size selection using SPRIselect Reagent (Beckman Coulter, B23317) to yield libraries containing P5 and P7 Illumina primer sequences, Sample indexes i5 and i7 (10x, 3000431), TruSeq Read 1 and 2 sites, 10x Barcode, Unique Molecular Identifier (UMI), and inserts. For scRNA-seq analysis of mouse livers, 3 generated libraries were pooled and sequenced in one lane on an Illumina HiSeq X instrument, generating a total of 367 million paired-end reads (read length of 2 x 150 = 300 bp). For scRNA-seq analysis of human HCC samples, 2 generated libraries were pooled and sequenced in one lane using the same sequencing platform and method.

Bulk RNA-seq analysis

The quality of sequencing reads was evaluated using FastQC. Adaptor sequences and low-quality score bases were trimmed using trimmomatic/0.39. The resulting reads were then mapped to the mouse reference sequence (GRCm38/mm10; Ensembl release 81) and counted using STAR 2.7.10a alignment software. Gene differential expression analysis was performed using the R package DESeq2[63]. Differential gene expression analysis was performed by comparing gene expression in $n = 3$ biologically independent *Ifih1*$^{-/-}$*Adar*$^{flox/flox}$ livers against $n = 3$ biologically independent *Ifih1*$^{-/-}$*Adar*$^{wt/wt}$ livers. Gene Ontology analysis was performed by using the Enrichr web tool,[56–58] using the top 50 DEGs based on top adjusted p-values (<0.05). Heatmap representation of top 50 DEG expression in $n = 3$ *Ifih1*$^{-/-}$*Adar*$^{wt/wt}$ livers, $n = 2$ *Ifih1*$^{-/-}$*Adar*$^{wt/flox}$ livers, and $n = 3$ *Ifih1*$^{-/-}$*Adar*$^{flox/flox}$ livers was performed using GraphPad, with normalization of each gene expression against that of *Ifih1*$^{-/-}$*Adar*$^{wt/wt}$ livers.

scRNA-seq data processing

The quality of sequencing reads was evaluated using FastQC. For mouse liver scRNA-seq experiments, Cell Ranger version 6.1.1 was used to align the sequencing reads (in FASTQ format) to the GRCm38/mm10 mouse transcriptome (version 2020-A) and quantify the expression of transcripts in each cell. This pipeline resulted in a gene expression matrix for each sample, which records the number of UMIs for each gene associated with each cell barcode. For human data, sequenced reads were aligned to the GRCh38 human transcriptome (version 2020-A). Unless otherwise stated, all downstream analyses were implemented using R version 4.1.2 and the package Seurat version 4.0.5[64]. For mouse liver scRNA-seq experiments, cells from three different conditions (*Ifih1*$^{-/-}$ *Adar*$^{wt/wt}$ *Ifih1*$^{-/-}$*Adar*$^{wt/flox}$ and *Ifih1*$^{-/-}$*Adar*$^{flox/flox}$) were pooled and analyzed together. After quality control, we obtained 27,985 high-quality cells with an average of 615 genes per cell. For 2 human samples (NT and Tumor), after excluding low-quality cells, a total of 18,885 cells with an average of 1,152 genes per cell were available for downstream analysis.

(1) *Batch correction*. The filtered cell-gene matrix was normalized with *NormalizeData* function and the 2000 feature genes selection was performed with VST method for *FindVariableFeatures*. To minimize technical variability due to sample collection while preserving biological variation, 2 functions in Seurat, *FindIntegrationAnchors* and *IntegrateData*, were used for batch correction among cells from three different conditions (*Ifih1*$^{-/-}$ *Adar*$^{wt/wt}$ *Ifih1*$^{-/-}$*Adar*$^{wt/flox}$ and *Ifih1*$^{-/-}$*Adar*$^{flox/flox}$). Specifically, 20 dimensions were used from the CCA to specify the neighbor search space, and all other arguments were kept by default.

(2) *Dimension reduction*. Dimension reduction includes 3 stages of analysis: selection of variable genes (*FindVariableFeatures*), PCA (*RunPCA*, from variable genes), and uniform manifold approximation and projection (*RunUMAP*). Specifically, we performed PCA using the 2,000 most variable genes selected by the *FindVariableFeatures*. The top 15 dimensions were selected as input features for UMAP to obtain bidimensional coordinates for each cell with min.pct argument as 0.3 and n.neighbors as 30. Notably, the batch-corrected data were only used for principal component analysis and the steps relying on PCA (for example, clustering and UMAP visualization). All other analyses (for example, differential expression analysis) were based on the normalized data without batch correction.

(3) *Unsupervised clustering and annotation*. *De novo* clustering was performed with FindNeighbors and FindClusters functions to cluster cells using the Louvain algorithm with random.seed argument as 42. The final number of cell clusters was determined

as 14 by selecting a resolution of 0.2. Next, scCATCH[65] version 2.1 was employed for cell type annotation of our mouse data with the selected tissues as ''Liver'', ''Fetal liver'', ''Blood'', ''Peripheral blood'', ''Serum'' and ''Umbilical cord blood''. For human data, scType[66] was used for cell type annotation with the selected tissues as "Liver" and "Immune system". To calculate the ISG score, a combined group of 8 ISGs (*Irf7*, *Ifit1*, *Isg15*, *Stat1*, *Ifitm3*, *Ifi44*, *Tgtp1*, *Ifnb1*) which were validated to be upregulated in *Ifih1*$^{-/-}$*Adar*$^{flox/flox}$ livers by qPCR were selected to define an ISG signature. The average normalized expression of these 8 ISGs was then calculated and defined as ISG score.

(4) *Identification of differential expressed genes (DEGs) from scRNA-seq data*. To identify DEGs, FindMarkers or FindAllMarkers functions (test.use = ''wilcox'', logfc.threshold = 0.25) were used based on normalized data. *P* value adjustment was performed with Bonferroni correction based on the total number of genes in the dataset. DEGs with adjusted *P* values > 0.05 were filtered out. Gene Ontology analysis was performed by using the Enrichr web tool,[56–58] or DAVID Bioinformatics Resources,[54,55] using top upregulated or downregulated significant DEGs (adjusted *P* value < 0.05, ranked by Log2FC) comparing respective cell types in *Ifih1*$^{-/-}$*Adar*$^{flox/flox}$ livers against *Ifih1*$^{-/-}$*Adar*$^{wt/flox}$ and *Ifih1*$^{-/-}$*Adar*$^{wt/wt}$ livers. Heatmap representation of relevant DEGs expression was performed using GraphPad by cross-referencing and plotting genes related to respective biological processes with normalization of each gene expression against that of *Ifih1*$^{-/-}$*Adar*$^{wt/wt}$ livers.

(5) *Trajectory inference for RNA velocity*. RNA velocity was analyzed with Scanpy, a scalable Python-based package (version 1.7.2) designed for single cell gene expression datasets. Using the output bam files from CellRanger *count*, we first sorted the bam files by cell-barcode using samtools *sort*. To annotate spliced and unspliced reads, we used the Velocyto pipeline[38] to generate corresponding loom files. The steady-state gene-specific velocities were computed and pre-processed following the scVelo python package.[67] Finally, we visualized the hepatocyte population on velocity *streamplot* and plotted the speed/rate for differentiation by the length of the velocity vector.

(6) *Cell-cell communication analysis by NicheNet*. To deeper understand intercellular cell to cell interaction for cell types of our interest, NicheNet[39] was employed to analyze the scRNA-seq data. This analysis utilized a large amount of public databases (such as KEGG, ENCODE, PhoshoSite) to track downstream effectors such as targets of transcription factors and receptors in the provided dataset. Three matrices, namely ''ligand-target prior model'', ''ligand-receptor network'' and ''weighted integrated networks'', are provided. When doing the communication analysis, receiver cell type was specified as ''Macrophage'' population and sender cell type as ''Hepatocyte'' population using the cell type labeled final Seurat object. And the condition of interest was selected as ''*Ifih1*$^{-/-}$*Adar*$^{flox/flox}$'' as compared to ''*Ifih1*$^{-/-}$*Adar*$^{wt/wt}$'' and ''*Ifih1*$^{-/-}$*Adar*$^{wt/flox}$''. The genes in the receiver/ligand cell populations are the ones that are differentially expressed upon inferred cell-cell interaction. More detailed NicheNet tutorials can be found in the GitHub page (https://github.com/saeyslab/nichenetr). Top intercellular pairs were identified by using the following filter criteria: genes expressed in >10% of respective cell type, and $Log_2FC > |0.25|$ and Wilcoxon rank-sum test *P*-value ≤ 0.05 for gene expression change in their respective cell type in *Ifih1*$^{-/-}$*Adar*$^{flox/flox}$ compared to that in *Ifih1*$^{-/-}$*Adar*$^{wt/wt}$ and *Ifih1*$^{-/-}$*Adar*$^{wt/flox}$ livers. Log_2FC, logarithmic transformation of gene fold change.

(7) *Immunophenotyping of macrophages. For subclustering of the macrophage population, UMI counts were re-scaled and dimension reduction was performed using the top 2000 most highly variable features for PCA and the first 10 principal components for UMAP.* Subclustering of the macrophage population yielded 8 clusters comprising of monocytes (*Ccr2, S100a4, S100a6*), Kupffer cells (*Clec4f, Vsig4, Timd4, Adgre1*), macrophages (*C1qa, C1qb, Fcgr3, Fabp5, Trem2*), cDC1 (*Xcr1, Clec9a, Cadm1, Btla, Wdfy4*) and proliferating myeloids (*Mki67, Hmgb2, Stmn1, Top2a*).[68] Classical and non-classical monocytes were annotated based on the presence and absence of *Ly6c2* respectively.[69] Presence of *Cd68* which is a resident marker,[70] *Cxc3cr1* which is implicated in monocyte differentiation into resident macrophages[71] and absence of Kupffer cell specific markers allowed us to annotate cluster 4 as recruited macrophages. A small population of *CD45*$^{+}$ cells expressed mixed signatures along with low levels of proliferation markers. They were annotated as 'mixed population' as the exact identity could not be determined. Differential gene expression analysis was performed using the FindAllMarkers() function in Seurat with parameters 'logfc.threshold = 0, pseudocount.use = 1' and the results were used for Gene Set Enrichment Analysis in Gene ontology ''biological process'' terms using the clusterProfiler R package gseGO() function (v4.6.2).[72]

(8) *Grn expression heatmap in scRNA sequencing showing expression across hepatocyte subclusters and mouse genotype*. We generated a heatmap to visualize the expression of the gene Grn across hepatocyte subclusters and samples using single-cell RNA sequencing (scRNA-seq) data. Briefly, the analysis began by extracting hepatocyte cells from the dataset and calculating pseudobulk average Grn expression values in normalized ''data'' slot grouped by sample identity and Seurat clusters using *AverageExpression()* function. The resulting expression data were processed to create a data frame with columns for sample identity, rows for cluster, and Grn expression values. Finally, after transforming the data into a wide format suitable for heatmap plotting, we generated the heatmap using the *heatmap.2()* function, with rows scaled to highlight relative expression level changes across the w/w, WT/Fl and Fl/Fl.

Spatial transcriptomics

Three sections per tissue were used for spatial transcriptomics analysis and the data shown are representative sections. Visium spatial gene expression kit (10x Genomics, 1000184) was used. Briefly, the livers of freshly euthanized mice were removed, cut into appropriately sized pieces, and embedded in OCT using an isopentane bath and liquid nitrogen. OCT sections were collected in a cryostat at 10μm thickness per section. Three sections of each tissue were collected onto mRNA capture slides. Only samples

with RIN >7 were used. Tissues were fixed in −20°C chilled methanol before H&E staining according to manufacturer's protocol (CG000160 Rev B). Tissue optimization as performed according to manufacturer's protocol to determine optimal permeabilization conditions (CG000238). Briefly, permeabilization enzyme was applied to H&E-stained tissues on optimization slide and a permeabilization time course was performed before fluorescent cDNA synthesis, tissue removal and slide imaging. All imaging was performed on EVOS M7000 imaging system (Thermo Fisher Scientific). Once optimal conditions were determined, tissue permeabilization was performed on Visium gene expression slides to release poly-adenylated mRNA from cells for capture by primers on ST spots underneath, followed by reverse transcription to generate barcoded full-length cDNA. cDNA was amplified and cleanup performed using SPRIselect Reagent (Beckman Coulter, B23317). Library preparation was performed according to manufacturer's protocol to generate libraries containing P5 and P7 Illumina primer sequences, Sample indexes i5 and i7 (10x, 3000431), TruSeq Read 1 and 2 sites, 10x Spatial Barcode, Unique Molecular Identifier (UMI), and inserts (CG000239 Rev D). A total of 9 generated libraries were pooled and sequenced in one lane using Novaseq-6000 S4 for a depth of 2.5B total Paired end reads.

To analyze sequenced spatially resolved Visium ST RNA-seq data, we applied the workflow introduced in Seurat v4[52]. Specifically, we removed the spots with number of detected genes less than 500, percentage of mitochondrial more than 10% and percentage of hemoglobin genes more than 10%. After removing mitochondrial genes and hemoglobin genes in the feature-cell matrix, SCTransform was performed to normalize the data and find variable genes. Next, we did dimensionality reduction with runPCA and clustering with FindClusters. Finally, to annotate each spot, we employed CellTrek[27] to chart single cells to their spatial locations. For *Grn-Egfr* co-expression analysis using ST data, only ST spots annotated to contain macrophages by CellTrek were considered for analysis. The expression of *Grn* and *Egfr* in such spots was then determined and the number of spots co-expressing both genes were quantified and presented as a percentage of total valid spots per tissue section.

QUANTIFICATION AND STATISTICAL ANALYSIS

Statistical analyses are listed in all figure legends and were performed in either GraphPad Prism 9, the R computing environment or Python computing environment. p values below 0.05 were considered statistically significant.